Received: 22 May 2022 | Revised: 9 December 2022 | Accepted: 22 December 2022 | Published on: 23 January 2023

DOI: 10.1002/qj.4425

Quarterly Journal of the Royal Meteorological Society

RESEARCH ARTICLE

On the intensification of typhoon *Damrey* with the monsoon gyre

Kexin Song[1] | **Li Tao**[1,2] | **Yang Yang**[3,4]

[1]School of Atmospheric Sciences/Collaborative Innovation Center on Forecast and Evaluation of Meteorological Disasters (CIC-FEMD), Nanjing University of Information Science & Technology, Nanjing, China

[2]State Key Laboratory of Severe Weather, Chinese Academy of Meteorological Sciences, Beijing, China

[3]School of Marine Sciences, Nanjing University of Information Science and Technology, Nanjing, China

[4]State Key Laboratory of Marine Environmental Science, College of Ocean and Earth Sciences, Xiamen University, Xiamen, China

Correspondence

Li Tao, School of Atmospheric Sciences, Nanjing University of Information Science & Technology, Nanjing, Jiangsu Province, 210044, China.
Email: taoli@nuist.edu.cn

Funding information

the Key Program of National Natural Science Foundation of China (NSFC), Grant/Award Number: 42230105; the Open Grants of the State Key Laboratory of Severe Weather, Grant/Award Number: 2022LASW-B07; the National Science Foundation of China (NSFC), Grant/Award Numbers: 42276017, 41975064

Abstract

Typhoon *Damrey*, the first named tropical cyclone (TC) of the year 2000 in the western North Pacific, was embedded in a monsoon gyre (MG) during its intensification period. We explored the mechanisms of its rapid development and the contribution of the MG using a localized, instantaneous energetics diagnostic tool: the multiscale window transform (MWT) and MWT-based multiscale energetics analysis. We used the ERA5 reanalysis dataset to obtain the fields on three temporal scales: TC-scale fields; MG-scale fields; and large-scale background fields. The canonical transfer of kinetic energy from the large-scale background fields to the tropical cyclone was negligible, whereas the MG increased the TC-scale kinetic energy in the precipitation active quadrant and weakened its kinetic energy in the precipitation inactive quadrant. Barotropic canonical transfer therefore did not contribute to the development of this tropical cyclone. Kinetic energy was produced in *Damrey* mainly through buoyancy conversion and pressure work. In the upper troposphere, the available potential energy converted to TC-scale kinetic energy, but this was mostly offset by the negative work done by the pressure gradient force with the updraught near the eyewall. In the lower troposphere, TC-scale kinetic energy was produced by horizontal pressure work due to the inflow. This new finding helps us to understand the impact of the MG on the TC intensification and the underlying mechanisms governing TC evolution.

KEYWORDS

canonical transfer, localized multiscale energetics, monsoon gyre, tropical cyclones

1 | INTRODUCTION

Tropical cyclones (TCs) often bring devastation to coastal communities. TCs are generated in tropical oceans and have a warm core and a non-frontal synoptic-scale cyclonic vortex with deep convection; they contain a large amount of energy. Classical theories about the mechanisms of the evolution of TCs include conditional instability of the second kind (CISK: Charney and Eliassen, 1964), the cooperative-intensification theory (Ooyama, 1969; 1982), wind-induced surface heat exchange (WISHE: Emanuel, 1986; 1989; 1997), balanced vortex dynamics (Schubert and Hack, 1982; Shapiro and Willoughby, 1982; Pendergrass and Willoughby, 2009;

Vigh and Schubert, 2009), and a vertical hot tower (Hendricks *et al.*, 2004; Montgomery *et al.*, 2006; 2009), etc.

The CISK theory suggests that the inflow in the boundary layer transports moisture into the inner core of the TC, resulting in cumulus convection in the inner core, the release of latent heat and spinning up of the vortex. However, the CISK theory is limited by the cumulus parametrization or closure problem, where convective heating is specified to be proportional to moisture convergence (Charney and Eliassen, 1964). Unlike the CISK theory, the cooperative-intensification theory (Ooyama, 1969; 1982) highlights the surface moisture convergence. And the WISHE theory suggests that the enhanced surface winds will increase the surface heat fluxes and adiabatic warming in the centre of the TC, leading to a lower pressure in the centre. The primary difference between the WISHE and CISK theory is closure. The WISHE theory links convective warming with the wind speed rather than moisture or frictional convergence (Craig and Gray, 1996). The azimuthally averaged secondary (overturning) circulation in TCs can be elegantly captured by balanced models (i.e. the Sawyer–Eliassen equation). However, balanced models significantly underestimate the low-level radial inflow (Bui *et al.*, 2009; Heng *et al.*, 2017) and the rapidly intensified TC generally needs to be treated as an unbalanced, perhaps nonlinear TC (Pendergrass and Willoughby, 2009).

Some studies suggested that the change in intensity of TCs is affected by both internal (Willoughby *et al.*, 1982; Wang, 2002; 2009; Houze *et al.*, 2007) and the external (environmental) processes, including the mid-tropospheric humidity and the vertical wind shear (Frank and Ritchie, 2001; Kaplan and DeMaria, 2003; Kaplan *et al.*, 2010; Riemer *et al.*, 2010; Tang and Emanuel, 2010; Chen *et al.*, 2015; Wood and Ritchie, 2015; Fowler and Galarneau, 2017; Ma *et al.*, 2019). Interactions between TCs and other nearby weather systems will affect their intensity and track. These weather systems include the synoptic-scale wave train (Hartmann and Maloney, 2001; Maloney and Hartmann, 2001), nearby TCs (Fujiwhara, 1921; 1923), monsoon troughs (Wu and Duan, 2015; Zong and Wu, 2015), upper tropospheric troughs (Hanley *et al.*, 2001; Leroux *et al.*, 2013), upper tropospheric cold lows (Yan *et al.*, 2021), intraseasonal oscillations (Maloney and Hartmann, 2001) and easterly waves (Molinari *et al.*, 2000). Larger-scale background fields, such as the subtropical high (Wang *et al.*, 2013; Wu *et al.*, 2020), also affect TCs.

It has been reported previously that monsoon gyres (MGs: Lander, 1994; 1996; Harr *et al.*, 1996) affect the track of TCs, which can experience sudden northward turning when they are embedded in an MG (Carr and Elsberry, 1995; Liang and Wu, 2015; Ge *et al.*, 2018). Some studies suggested that MGs can modulate the intensity of TCs (Liang *et al.*, 2016; 2018a; 2018b; Yan *et al.*, 2019; Song *et al.*, 2021). Based on a statistical analysis of the Joint Typhoon Warning Center (JTWC) dataset, Liang *et al.* (2018a) and Song *et al.* (2021) found that TCs are more likely to incur rapid weakening when they are embedded in an MG. Liang *et al.* (2016; 2018b) found that MGs affected the change in intensity of typhoon *Chan-Hom* (2015) by modulating the transport of mass and moisture into the TC. Based on an idealized numerical experiment, Yan *et al.* (2019) found that the development of TCs is slower when they are embedded in an MG and that MGs affect the intensity of TCs through vorticity segregation processes, barotropic instability and the modulation of vertical wind shear.

In this study, we investigated the extent to which the barotropic energy of the MG contributes to the development of TCs using the multiscale window transform (MWT: Liang, 2002; Liang and Anderson, 2007) and MWT-based multiscale energy and vorticity analysis (MS-EVA: Liang and Robinson, 2005; 2007; Liang, 2016) to the first named TC of the year 2000 over the western North Pacific (typhoon *Damrey*), which was embedded in an MG during its intensification. The traditional temporally or spatially averaged energy diagnostic approach is not suitable for TCs, which are highly localized and rapidly developing weather systems. Liang and Anderson (2007) and Liang (2016) overcame this difficulty by introducing MWT and MS-EVA, which can determine the transfer and transport of energy between multiscale systems without using the temporal or spatial average. The sum of the energy transferred is zero over scale windows, indicating that it is simply a redistribution of energy among these windows, referred to as canonical transfer by Liang and Anderson (2007). The MWT and MS-EVA methods have been applied to mean-eddy interactions in the ocean (Liang and Robinson, 2009; Yang and Liang, 2016), blocking highs (Ma and Liang, 2017), sudden stratospheric warming (Xu and Liang, 2017), the extreme freezing event in North America in January 2019 (Xu and Liang, 2020) and the development of TCs (Wang and Liang, 2017; Xu and Liang, 2022), etc. We applied this method to investigate the rapid development mechanisms of typhoon *Damrey* and the contribution of the MG. Figure 1 shows that *Damrey* formed in the western North Pacific northeast of Palau on 5 May 2000, then moved northwest before suddenly turning northeast on 8 May. It reached its maximum intensity at 1800 UTC on 9 May, then gradually weakened to a tropical depression on 13 May. We explored the kinetic energy and energy transfer and transform processes during the development of *Damrey*, especially focused on the contributions of the MG-scale and the background systems to the intensification of *Damrey*.

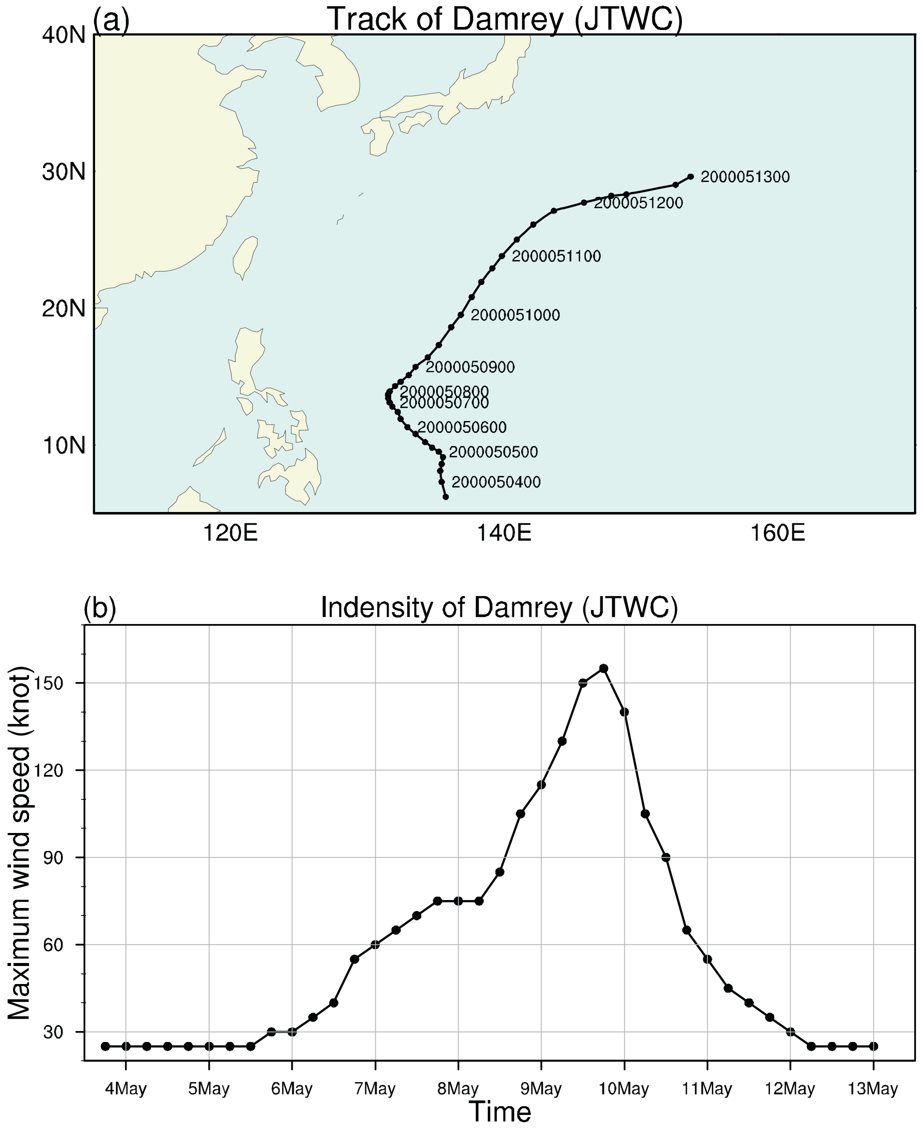

FIGURE 1 (a) Track of typhoon *Damrey* from the JTWC dataset. (b) Variation in the intensity of *Damrey* over time based on the maximum 1 min average sustained surface wind speed from the JTWC dataset [Colour figure can be viewed at wileyonlinelibrary.com]

The rest of the article is organized as follows. Section 2 briefly describes the data and methods used. Section 3.1 sets the MWT parameters and reconstructs typhoon *Damrey* in the synoptic-scale window with MWT. Multiscale energetics analysis is discussed in Section 3.2 and our conclusions are given in Section 4.

2 | DATA AND METHODS

The best-track data for typhoon *Damrey* were from the JTWC with a time interval of 6 hr and included the maximum 1 min average sustained surface wind speed and the location of the TC centre (longitude and latitude). The 6 hr reanalysis data from the Fifth Generation European Centre for Medium-Range Weather Forecasts reanalysis dataset (ERA5: Hersbach *et al.*, 2020) were used for energy analysis and included the zonal and meridional winds, the geopotential height, temperature and precipitation with a horizontal resolution of $(0.25° \times 0.25°)$ at 37 pressure levels.

We chose a time span from 0000 UTC on 25 February to 1800 UTC on 6 November 2000, which gives a total of 1024 $\left(2^{10}\right)$ time steps. We chose this time span because it is long enough to avoid possible boundary effects and the number of time steps of the input data is a power of two, as required by MWT analysis. In order to explore the contribution of various scale systems to the change in intensity of *Damrey*, we decomposed and reconstructed the total field into three temporal scales by applying MWT: a background window (>64 days); an MG-scale window (16–64 days); and a TC-scale window (<16 days). For easy reference, the three scale windows are denoted as $\varpi = 0, 1, 2$, respectively. The 6 hr ERA5 dataset with 128 days (512 time steps) were also applied, which span from 0000 UTC on 26 March to 1800 UTC on 31 July 2000, to decompose the dataset into the large-scale, the MG-scale, and the TC-scale circulations with MWT. The results are the same (as shown in Figure S1). The dataset less than 64 days (256 time steps) cannot be used in this study because the large-scale background circulations defined are longer than 64 days.

MWT was developed by Liang (2002) to diagnose localized energy process between three or more scales. Liang (2002) constructed an orthonormal scaling basis $\phi_n^{\varrho,j}(t)$ based on the orthonormalization cubic spline.

For any function $T(t) \in L_2[0,1]$ ($L_2[0,1]$ represents the space of square integrable functions defined on [0,1]), it can be written as:

$$T(t) = \sum_{j=0}^{+\infty} \sum_{n=0}^{2^j \varrho - 1} \tilde{T}_n^j \psi_n^{\varrho,j}(t), t \in [0,1], \tag{1}$$

where

$$\psi_n^{\varrho,j}(t) = \sum_{\ell=-\infty}^{+\infty} 2^{j/2} \psi \left(2^j (t + \varrho \ell) - n \right), \quad n = 0, 1, \dots, 2^j \varrho - 1. \tag{2}$$

$\psi_n^{\varrho,j}(t)$ is some orthonormal wavelet function constructed via orthonormalization cubic spline (cf. Figure 1a in Liang and Robinson (2005)), j representing scale level (2^{-j} is the scale), n the time step, $\varrho = 1$ and $\varrho = 2$ corresponding to the periodic and symmetric extension schemes, respectively. In Equation (1), the group of certain range of scale levels, say, $j_1, j_1 + 1, \dots, j_2$ form the subspace of $L_2[0,1]$, which is called a scale window. Any function in $L_2[0,1]$, say $T(t)$, can be decomposed into a sum of several windows. Specifically for this work, we define three scale windows: large-scale window ($0 \le j \le j_0 = 3$), MG-scale window ($j_0 < j \le j_1 = 5$), and TC-scale window ($j_1 < j \le j_2 = 10$). j_2 corresponds to the finest resolution (sampling interval 2^{-j_2}).

Due to orthonormal wavelet transform coefficients being defined discretely on different locations for different scales, Liang (2002) make a direct sum of subspaces spanned by the wavelet basis $\left\{\psi_n^m(t)\right\}_n$, for all $m \le j$, and get orthonormal translation invariant basis $\phi_n^j(t)$ (cf. Figure 1a in Liang and Robinson (2005)) in company with the wavelet function $\psi(t)$.

Given a time series $T(t) \in L_2[0,1]$, write:

$$\hat{T}_n^j = \int_0^{\varrho} T(t) \phi_n^{\varrho,j}(t) dt, \text{for all } 0 \le j \le j_2, \quad n = 0, 1, \dots, 2^j \varrho - 1. \tag{3}$$

For window bounds $j_0 < j_1 < j_2$, three functions can be accordingly defined:

$$T^{\sim 0}(t) = \sum_{n=0}^{2^{j_0} \varrho - 1} \hat{T}_n^{j_0} \phi_n^{\varrho,j_0}(t), \tag{4}$$

$$T^{\sim 1}(t) = \sum_{n=0}^{2^{j_1} \varrho - 1} \hat{T}_n^{j_1} \phi_n^{\varrho,j_1}(t) - T^{\sim 0}(t), \tag{5}$$

$$T^{\sim 2}(t) = T(t) - \sum_{n=0}^{2^{j_1} \varrho - 1} \hat{T}_n^{j_1} \phi_n^{\varrho,j_1}(t), \tag{6}$$

where the symbols ~0, ~1, ~2 denote three scale windows. With these reconstructions, the multiscale window transformation of $\hat{T}_n^{\sim\varpi}$ is defined as:

$$\hat{T}_n^{\sim\varpi} = \int_0^{\varrho} T^{\sim\varpi}(t) \phi_n^{\varrho,j_2}(t) dt, \text{for } \varpi = 0, 1, 2, \quad \text{and } n = 0, 1, \dots, 2^{j_2} \varrho - 1. \tag{7}$$

And the reconstructions on the above three windows can be written uniformly as:

$$T^{\sim\varpi}(t) = \sum_{n=0}^{2^{j_2} \varrho - 1} \hat{T}_n^{\sim\varpi} \phi_n^{\varrho,j_2}(t), \text{for } \varpi = 0, 1, 2. \tag{8}$$

Unlike traditional filters, MWT yields not only reconstructions (i.e. filtered fields), but also transform coefficients, which are essential to define the energy associated with a filtered field. The energy of T on scale window ϖ at step n is:

$$E_n^{\varpi} = 2^{j_2} \left(\hat{T}_n^{\sim\varpi} \right)^2. \tag{9}$$

The subscript n denotes the discrete time step in the sampling space, which is omitted hereafter for brevity. Note that it is not simply the square of the filtered field (i.e. $[T^{\sim\varpi}]^2$), as commonly used in the literature. For more details, refer to Liang (2002), Liang and Robinson (2005), Liang and Anderson (2007) and Liang (2016).

The kinetic energy equation on the scale window ϖ ($\varpi = 0, 1, 2$) (Liang and Robinson, 2005; Liang, 2016) is:

$$\frac{\partial K^{\varpi}}{\partial t} + \nabla \cdot Q_K^{\varpi} = \Gamma_K^{\varpi} - \nabla \cdot Q_P^{\varpi} - b^{\varpi} + F_K^{\varpi}. \tag{10}$$

Here

$$\Gamma_K^{\varpi} = \frac{1}{2} \left\{ \left(\widehat{\boldsymbol{V}\boldsymbol{V}_h} \right)^{\sim\varpi} : \nabla \hat{\boldsymbol{V}}_h^{\sim\varpi} - \left[\nabla \cdot \left(\widehat{\boldsymbol{V}\boldsymbol{V}_h} \right)^{\sim\varpi} \right] \cdot \hat{\boldsymbol{V}}_h^{\sim\varpi} \right\}, \tag{11}$$

$$\begin{aligned} Q_k^{\varpi} = & \frac{1}{2} \left(\widehat{uu}^{\sim\varpi} \hat{u}^{\sim\varpi} + \widehat{uv}^{\sim\varpi} \hat{v}^{\sim\varpi} \right) \\ & + \frac{1}{2} \left(\widehat{vu}^{\sim\varpi} \hat{u}^{\sim\varpi} + \widehat{vv}^{\sim\varpi} \hat{v}^{\sim\varpi} \right) \\ & + \frac{1}{2} \left(\widehat{\omega u}^{\sim\varpi} \hat{u}^{\sim\varpi} + \widehat{\omega v}^{\sim\varpi} \hat{v}^{\sim\varpi} \right), \end{aligned} \tag{12}$$

$$\nabla\cdot Q_P^{\varpi}=\frac{\partial\left(\widehat{u}^{\sim\varpi}\widehat{\Phi}^{\sim\varpi}\right)}{\partial x}+\frac{\partial\left(\widehat{v}^{\sim\varpi}\widehat{\Phi}^{\sim\varpi}\right)}{\partial y}+\frac{\partial\left(\widehat{\omega}^{\sim\varpi}\widehat{\Phi}^{\sim\varpi}\right)}{\partial p},\tag{13}$$

$$b^{\varpi}=\widehat{\omega}^{\sim\varpi}\widehat{\alpha}^{\sim\varpi},\tag{14}$$

where K^{ϖ} is the kinetic energy on window ϖ, Γ_K^{ϖ} is the canonical energy transfer to window ϖ, Q_K^{ϖ} is the flux of kinetic energy on scale window ϖ, Q_P^{ϖ} is the geopotential flux, b^{ϖ} is the buoyancy conversion between the kinetic energy and the available potential energy (APE) on window ϖ and F_K^{ϖ} is the dissipation. Φ is the geopotential and α is specific volume; the other symbols are conventional. $\widehat{()}^{\sim\varpi}$ is the MWT transform coefficient on scale window ϖ at time step n and the subscript n is omitted for brevity. The colon operator is defined such that for two dyadic products $\boldsymbol{AB}$ and $\boldsymbol{CD}$,

$$(\boldsymbol{AB}):(\boldsymbol{CD})=(\boldsymbol{A}\cdot\boldsymbol{C})(\boldsymbol{B}\cdot\boldsymbol{D}).\tag{15}$$

Equation (11) on scale window ϖ at step n is generally understood as:

$$\begin{aligned}\Gamma_K^{\varpi}=\frac{1}{2}\Bigg\{&\left(\widehat{uu}^{\sim\varpi}\frac{\partial\widehat{u}^{\sim\varpi}}{\partial x}+\widehat{vu}^{\sim\varpi}\frac{\partial\widehat{u}^{\sim\varpi}}{\partial y}+\widehat{\omega u}^{\sim\varpi}\frac{\partial\widehat{u}^{\sim\varpi}}{\partial p}\right)\\&-\left[\widehat{u}^{\sim\varpi}\left(\frac{\partial\widehat{uu}^{\sim\varpi}}{\partial x}+\frac{\partial\widehat{vu}^{\sim\varpi}}{\partial y}+\frac{\partial\widehat{\omega u}^{\sim\varpi}}{\partial p}\right)\right]\Bigg\}\\&+\frac{1}{2}\Bigg\{\left(\widehat{uv}^{\sim\varpi}\frac{\partial\widehat{v}^{\sim\varpi}}{\partial x}+\widehat{vv}^{\sim\varpi}\frac{\partial\widehat{v}^{\sim\varpi}}{\partial y}+\widehat{\omega v}^{\sim\varpi}\frac{\partial\widehat{v}^{\sim\varpi}}{\partial p}\right)\\&-\left[\widehat{v}^{\sim\varpi}\left(\frac{\partial\widehat{uv}^{\sim\varpi}}{\partial x}+\frac{\partial\widehat{vv}^{\sim\varpi}}{\partial y}+\frac{\partial\widehat{\omega v}^{\sim\varpi}}{\partial p}\right)\right]\Bigg\}.\end{aligned}\tag{16}$$

All the terms on the right-hand side of Equation (16) can be written as a linear combination of terms in the following triple product form:

$$\Gamma_K^{\varpi}=\widehat{R}^{\sim\varpi}\widehat{pq}^{\sim\varpi}.\tag{17}$$

For a three-window decomposition $\varpi=0,1,2$, taking $\varpi=2$ (a window on TC scale) as an example, Γ_K^2 can be decomposed as:

$$\begin{aligned}\Gamma_K^{\varpi}=\Gamma_K^2=\widehat{R}^{\sim2}\widehat{pq}^{\sim2}&=\widehat{R}^{\sim2}\widehat{\left(\sum_{\varpi_1=0}^{2}p^{\sim\varpi_1}\sum_{\varpi_2=0}^{2}q^{\sim\varpi_2}\right)}^{\sim2}\\&=\widehat{R}^{\sim2}\left[\left(\widehat{p^{\sim0}q^{\sim0}}\right)^{\sim2}+\left(\widehat{p^{\sim0}q^{\sim2}}\right)^{\sim2}+\left(\widehat{p^{\sim2}q^{\sim0}}\right)^{\sim2}\right]\\&\quad+\widehat{R}^{\sim2}\left[\left(\widehat{p^{\sim1}q^{\sim1}}\right)^{\sim2}+\left(\widehat{p^{\sim1}q^{\sim2}}\right)^{\sim2}+\left(\widehat{p^{\sim2}q^{\sim1}}\right)^{\sim2}\right]\\&\quad+\widehat{R}^{\sim2}\left[\left(\widehat{p^{\sim0}q^{\sim1}}\right)^{\sim2}+\left(\widehat{p^{\sim1}q^{\sim0}}\right)^{\sim2}\right]+\widehat{R}^{\sim2}\left[\left(\widehat{p^{\sim2}q^{\sim2}}\right)^{\sim2}\right].\end{aligned}\tag{18}$$

The first term $\widehat{R}^{\sim2}\left[\left(\widehat{p^{\sim0}q^{\sim0}}\right)^{\sim2}+\left(\widehat{p^{\sim0}q^{\sim2}}\right)^{\sim2}+\left(\widehat{p^{\sim2}q^{\sim0}}\right)^{\sim2}\right]=\Gamma_K^{0\to2}$ is the energy transfer from scale window 0 to scale window 2. The second term $\widehat{R}^{\sim2}\left[\left(\widehat{p^{\sim1}q^{\sim1}}\right)^{\sim2}+\left(\widehat{p^{\sim1}q^{\sim2}}\right)^{\sim2}+\left(\widehat{p^{\sim2}q^{\sim1}}\right)^{\sim2}\right]=\Gamma_K^{1\to2}$ is the energy transfer from window 1 to window 2. The third term $\widehat{R}^{\sim2}\left[\left(\widehat{p^{\sim0}q^{\sim1}}\right)^{\sim2}+\left(\widehat{p^{\sim1}q^{\sim0}}\right)^{\sim2}\right]=\Gamma_K^{0\oplus1\to2}$ is the combined contribution to Γ_K^2 from the two-scale window 0 and window 1, which is generally negligible. The last term $\widehat{R}^{\sim2}\left[\left(\widehat{p^{\sim2}q^{\sim2}}\right)^{\sim2}\right]=\Gamma_K^{2\to2}$ is the canonical energy transfer from window 2 itself. In particular, Γ_K^{ϖ} has a very important property, which has been rigorously proved by Liang (2016):

$$\sum_{\varpi}\left(\sum_{n}\Gamma_K^{\varpi}\right)=0.\tag{19}$$

This means that Γ_K^{ϖ} is simply a redistribution of kinetic energy among the scale windows without creating or consuming any energy. To distinguish it from the terms in previously published work, Γ_K^{ϖ} is referred to as canonical transfer (Liang, 2016). More details are available in Liang (2016). The software for MWT and MS-EVA and related references can be downloaded from the website http://www.ncoads.org/.

Because TCs are moving weather systems, we did not analyse the flux of kinetic energy in this study. Equation (10) can therefore be rewritten as:

$$\frac{dK^{\varpi}}{dt}=\Gamma_K^{\varpi}-\nabla\cdot Q_P^{\varpi}-b^{\varpi}+F_K^{\varpi},\tag{20}$$

where $\varpi=2$, Γ_K^{ϖ} is the kinetic energy (canonical energy) transfer from background and MG-scale circulations to TC-scale circulation, which represents the barotropic instability. $-\nabla\cdot Q_P^{\varpi}$ is the work done by the pressure gradient force, which is related to the inflow and the pressure gradient. $-b^{\varpi}$ is the buoyancy conversion from the TC-scale available potential energy to the TC-scale kinetic energy, which is related to the ascending of warmer air or the sinking of colder air. We only analysed the first three terms on the right-hand side of Equation (20).

In the following section, we investigated the transfer of energy between the MG and typhoon *Damrey* during its intensification phase to understand the contribution of the MG to the development of the typhoon and the underlying mechanisms governing TC intensification.

3 | RESULTS

3.1 | Multiscale reconstruction with MWT

Typhoon *Damrey* was embedded in an MG, which has a larger-scale cyclonic circulation than a TC with a duration of 2 to 3 weeks. We decomposed and reconstructed the total fields from the ERA5 reanalysis dataset into three temporal scales using MWT: the TC-scale circulation (<16 days); the MG-scale circulation (16–64 days); and the background circulation (>64 days).

Because the centre of *Damrey* in the ERA5 dataset was different from that in the JTWC observations, we had to determine the centre of the TC in the ERA5 dataset. We identified the location of the minimum wind speed at 850 hPa within 200 km of the centre of the TC in the JTWC dataset as the centre of *Damrey* in the ERA5 dataset (Figure 2, red dots). The red circles in Figure 2 are the circular range 150 km from the centre of the TC in the ERA5 dataset. The wind swirl patterns show that the centre of the TC determined here is reasonable.

Figure 3 shows the 16–64-day circulation at 850 hPa. The development of *Damrey* was accompanied by a larger-scale MG circulation. At the initial time, *Damrey* was located in the south of the MG. There was no obvious change in the position of the MG, while *Damrey* then moved northeast. At 0600 UTC on 9 May, the centre of the TC roughly coincided with the centre of the MG. *Damrey* was located in the northeast of the MG on 10 May and then moved out of the MG.

Figure 4 shows wind and vorticity at 850 hPa (first row), 200 hPa (second row), geopotential height at 1000 hPa (third row), temperature at 500 hPa (fourth row) and omega at 500 hPa (fifth row) on the scale of 16–64 days. On 7 May, the MG was a quasi-circular cyclonic circulation at low level, with high positive vorticity in its centre and along *Damrey*'s track (Figure 4, first row), which were concurrent with the low pressure at 1,000 hPa (Figure 4, third row). The MG gradually elongated in an east–west direction and became an elliptical circulation. At 200 hPa, an anticyclonic circulation was located in the east of the cyclonic circulation at 850 hPa. Moreover, the MG had a warm centre and upward motion at 500 hPa. In the MG's northeastern and southeastern quadrants, the upward motion was prominent. The baroclinic structure of the MG is consistent with previous studies (Wu *et al.*, 2013; Song *et al.*, 2021).

Figure 5 shows the circulation of the >64-day circulation, which represents the large-scale background. This circulation pattern includes the subtropical high and westerly jet at midlatitudes. *Damrey* moved along the periphery of the subtropical high and then entered the westerly jet at mid- and upper layers during and after 10 May (Figure 5a,b). The red line in Figure 5 represents the trajectory of the TC obtained from the TC-scale circulation in the ERA5 dataset and the black line represents the trajectory of the TC obtained from the JTWC dataset. These two trajectories are almost coincident.

3.2 | Multiscale energetics analysis

3.2.1 | Evolution of the kinetic energy on the TC scale

Figure 6 shows the time–pressure cross-section of the kinetic energy on the TC scale averaged over a circle with a 150 km radius away from the centre of the TC and the time series of the vertically integrated kinetic energy on the same scale. The kinetic energy of typhoon *Damrey* increased rapidly before 0600 UTC on 9 May and the vertically integrated kinetic energy reached a maximum at 1800 UTC on 9 May, after which time the kinetic energy began to weaken top down from 400 hPa. The results averaged over the circle of radius 100 km (Figure S2) are consistent with the above results, except the intensity of kinetic energy is less and the vertically integrated kinetic energy reaching a maximum was 12 hr earlier. The maximum sustained wind speed of *Damrey* increased more than 30 kt (1 knot = 0.514 $\mathrm{m \cdot s^{-1}}$) in 24 hr (95th percentile of 24 hr intensity changes for TCs in the western North Pacific) from 0600 UTC on 8 May to 0600 UTC on 9 May (Figure 1b), which is the rapid intensification period of *Damrey*.

The following section analyses the mechanism of *Damrey*'s intensification and explores the contribution of the MG. We focus on the time period from 1200 UTC on 7 May to 1800 UTC on 9 May – that is, the time period between the red dashed lines in Figure 6. For simplicity, some figures at 0000 and 1200 UTC are not shown here because they are consistent with those at 0600 and 1800 UTC.

3.2.2 | Characteristics of the TC

We sectioned the TC based on the distribution of precipitation around the centre of the TC to show its profile. Figure 7 shows that the precipitation was initially asymmetrically distributed around the centre of the TC, but became more axisymmetric at 1200 UTC on May 9. The precipitation moved counter-clockwise with time in the tangential direction. On 7 May, precipitation occurred in the northwest of the TC and then moved from the southwest to the south on 8 May. Precipitation occurred in the east of the TC from 1200 to 1800 UTC on 9 May. In the radial direction, the precipitation was mainly distributed within a 300 km radius of the centre of the TC.

The distributions of precipitation during intensification of the TC (Figure 7) were consistent with the vertical velocity at 500 hPa (Figure S3) – that is, significant upward movement usually occurred in areas with a large amount of precipitation. We determined the area of active precipitation (the area of the 90° quadrant between the two solid black lines; Figure 7) and the area of inactive

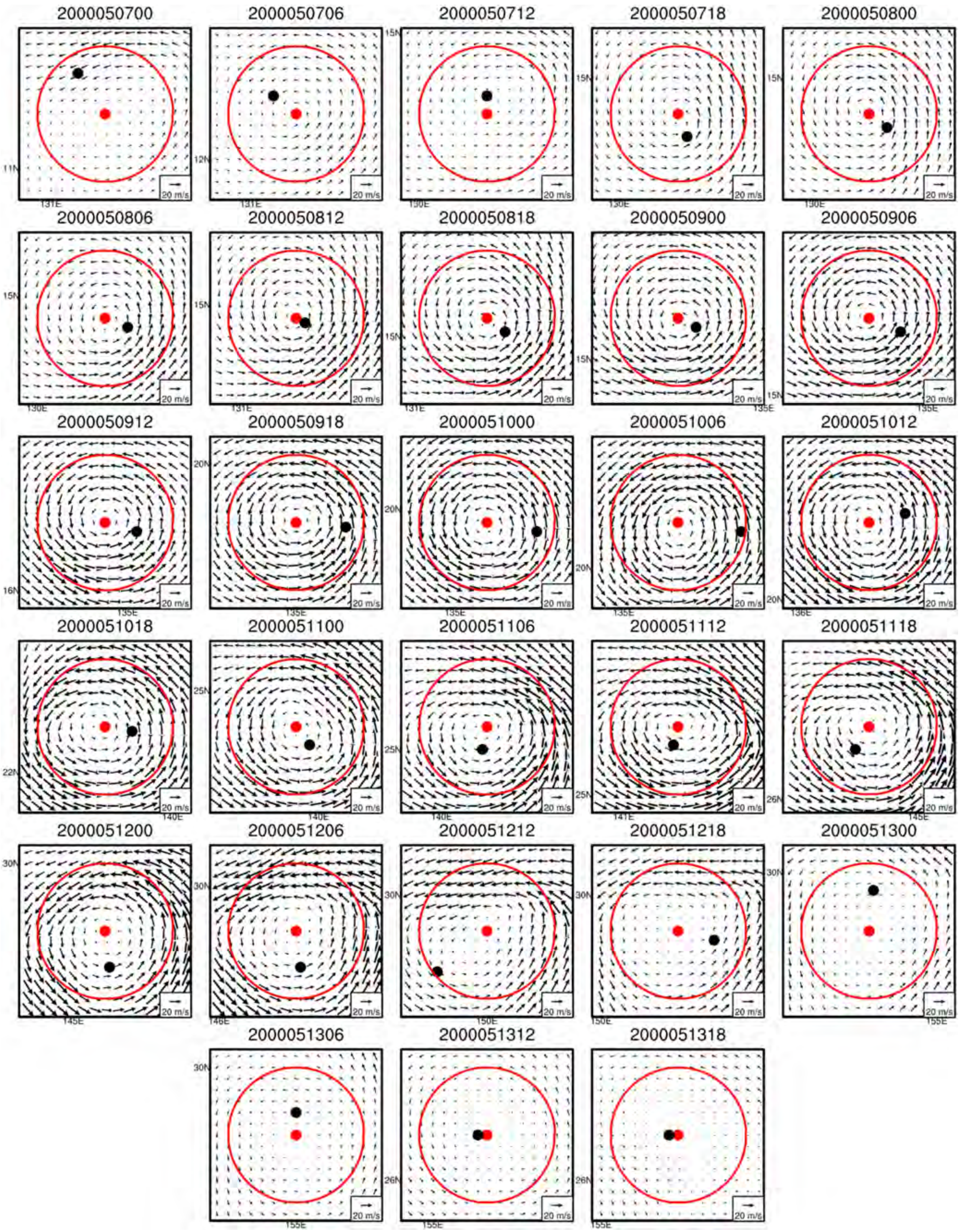

FIGURE 2 The 850 hPa wind field on the TC scale (<16 days) obtained using MWT. The red (black) dots are the centre of the TC in the ERA5 dataset (JTWC observations). The red circles represent a circle with a radius of 150 km centred on the TC [Colour figure can be viewed at wileyonlinelibrary.com]

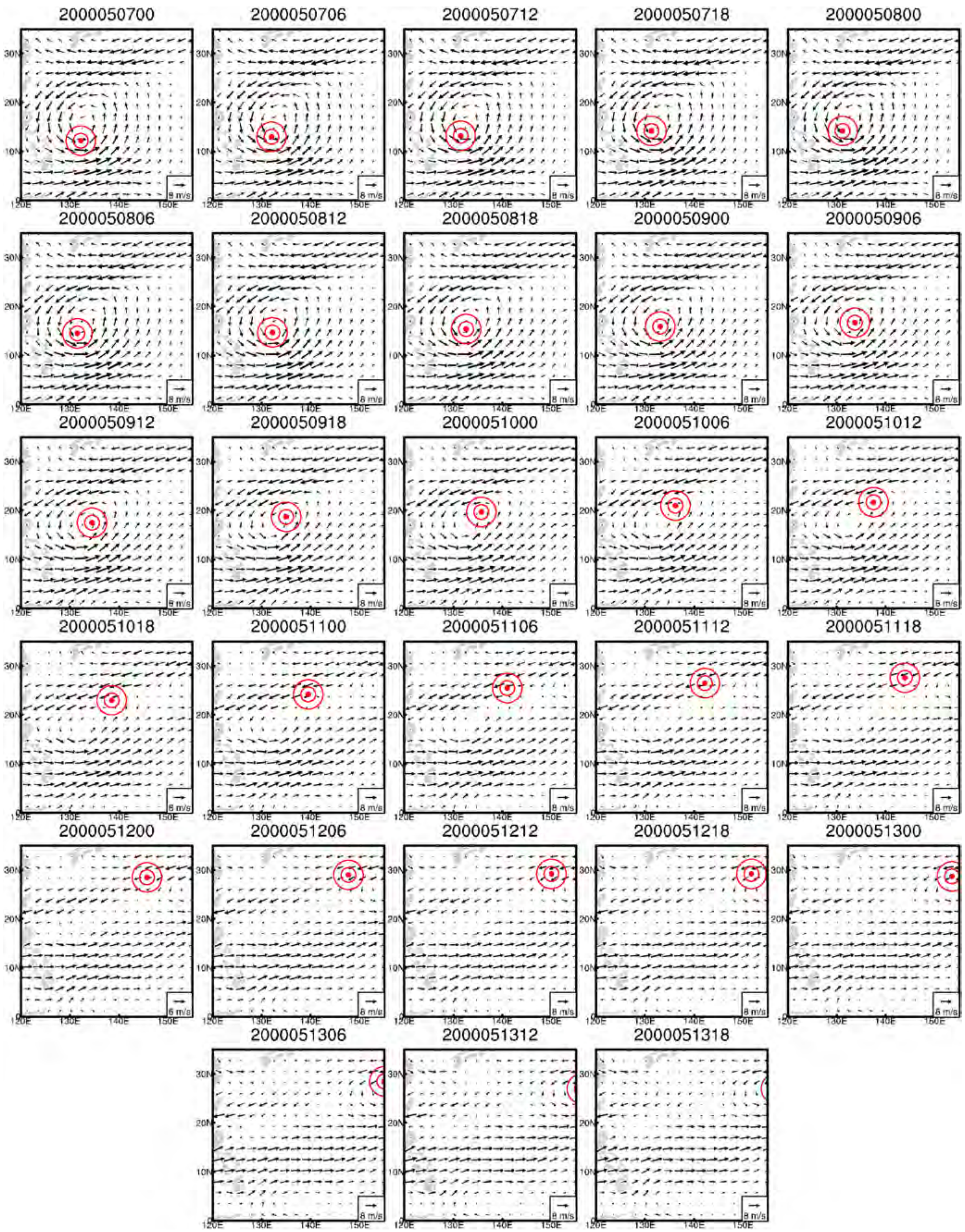

FIGURE 3 The 850 hPa wind field on the MG scale (16–64 days). The red dots are the centre of *Damrey* in the ERA5 dataset. The red circles are circles with a radius of 150 and 300 km from the centre of the TC in the ERA5 dataset [Colour figure can be viewed at wileyonlinelibrary.com]

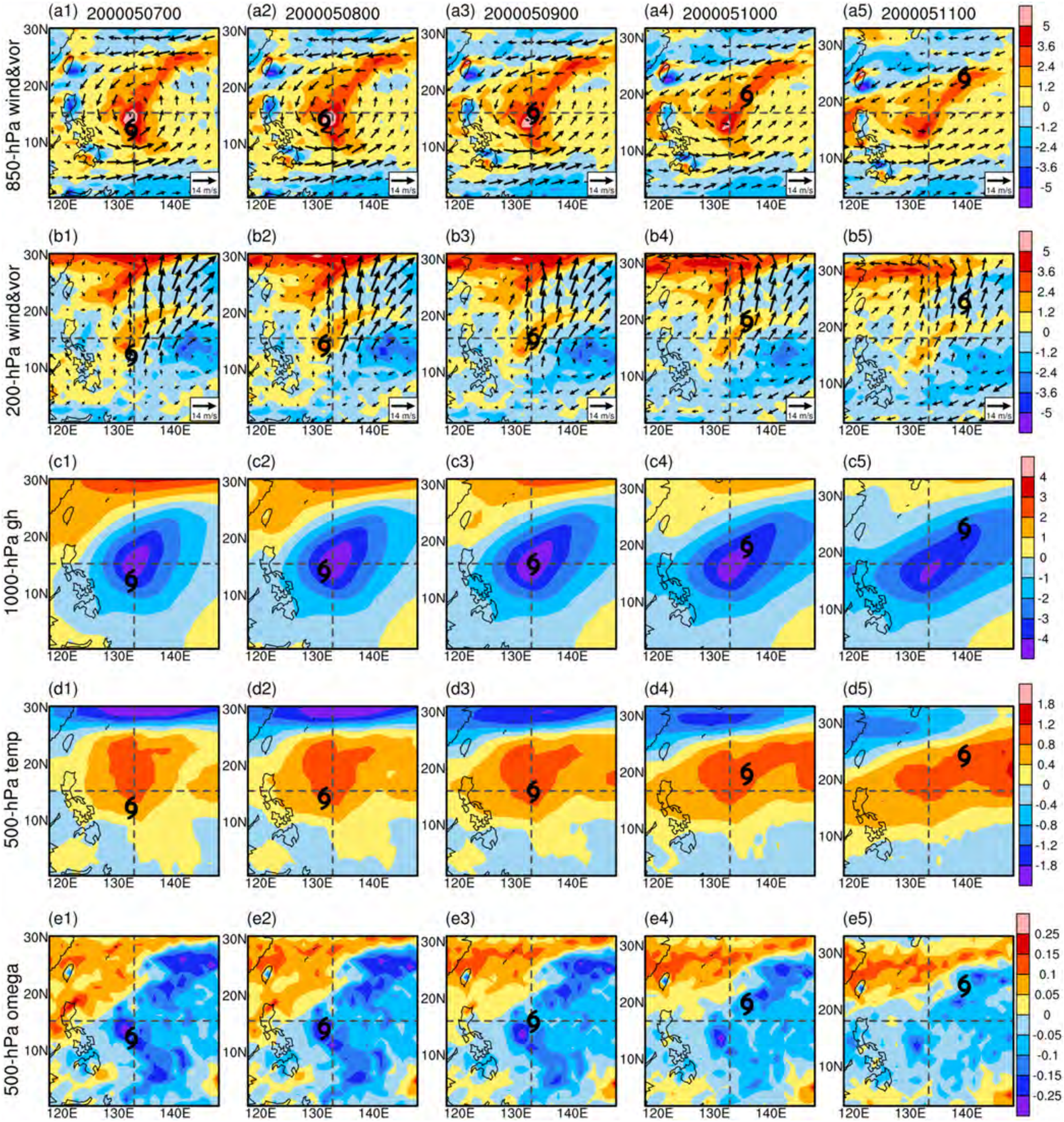

FIGURE 4 Daily horizontal wind (vectors; m·s^{-1}) and relative vorticity (shadings; 10^{-5} s^{-1}) at 850 hPa (a1–a5) and 200 hPa (b1–b5), geopotential height at 1000 hPa (c1–c5; m^2·s^{-2}), temperature at 500 hPa (d1–d5; K) and omega at 500 hPa (e1–e5; Pascal·s^{-1}) on the MG scale (16–64 days) obtained by using MWT. All figures are centred at the 850 hPa centre of the MG. The typhoon symbols are the *Damrey*'s centre in the ERA5 dataset [Colour figure can be viewed at wileyonlinelibrary.com]

precipitation (the diagonal area; Figure 7) basically based on the precipitation intensity, that is, the maximum value of the precipitation was taken as the centre of a 90° quadrant and the quadrant was defined as the active quadrant; the diagonal 90° quadrant was the inactive quadrant. Moreover, considering the motion continuity, we slightly adjusted it according to 500 hPa vertical velocity at 0600 UTC on 7 May, 0800 UTC on 8 May, and 1800 UTC on 9 May, so that the active quadrant moved counter-clockwise with time.

Figure 8 shows vertical cross-sections of the vertical *p*-velocity, horizontal wind and temperature anomalies on

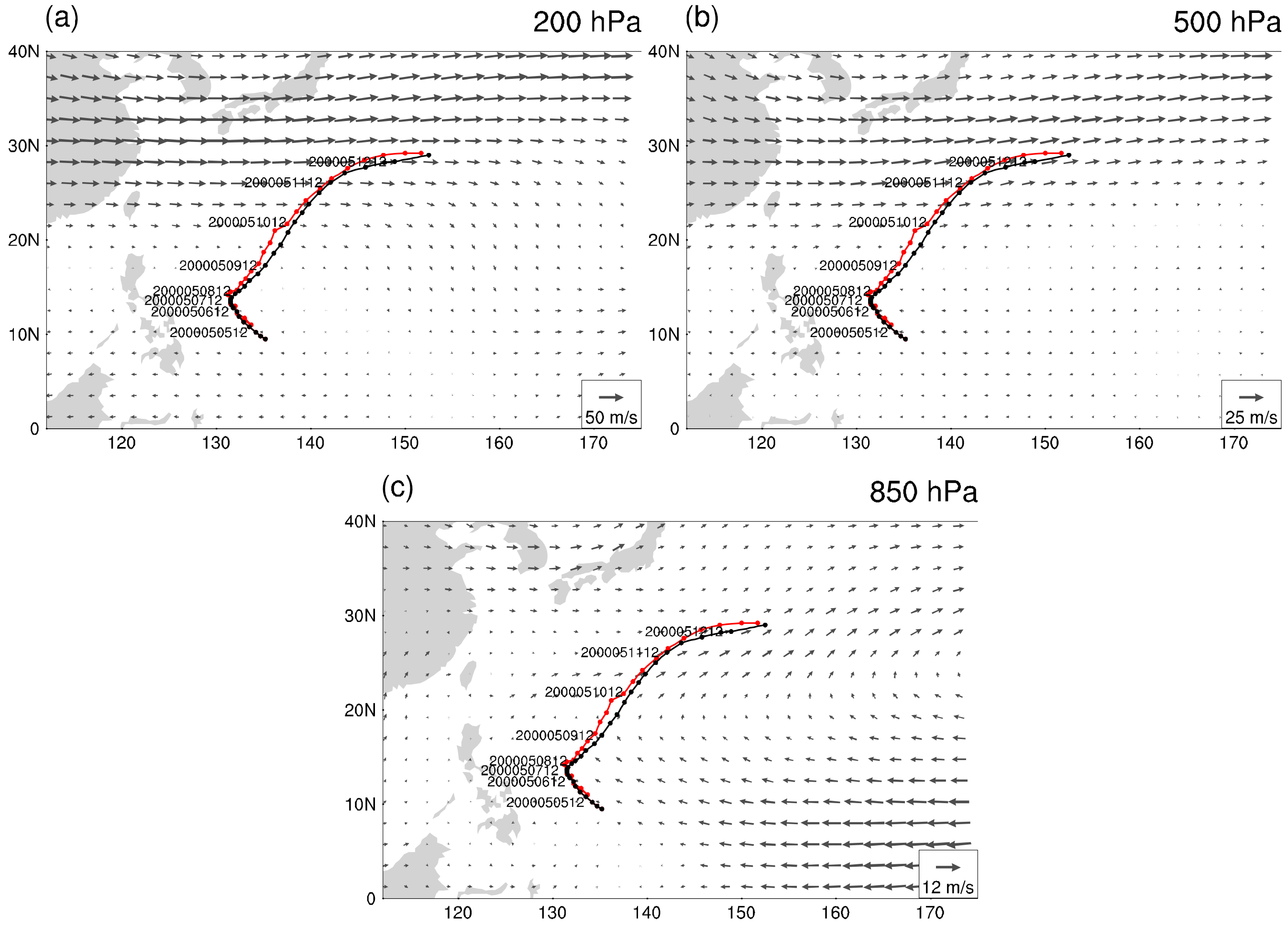

FIGURE 5 The wind fields of the large-scale background (>64 day) during life span of *Damrey* (from 5 to 12 May 2000) at (a) 200 hPa, (b) 500 hPa and (c) 850 hPa. The red lines are the trajectories of *Damrey* with the centre determined in the ERA5 dataset and the black lines are its trajectories with the centre determined in the JTWC dataset [Colour figure can be viewed at wileyonlinelibrary.com]

the TC scale averaged over the 90° active and inactive quadrants centred on the TC. The right-hand panels show the active region and the left-hand panels show the inactive region. Figure 8 shows that there was obvious upward motion around the centre of the TC, but the updraught was clearly asymmetrical and much more intense in the active quadrant. The downdraught was inside the eyewall of the TC, with the maximum downdraught at 300 hPa, which means that the sky was clear and cloudless in the TC eye (Figure 8a–e). There was some downdraught outside the eye of the TC below the mid-level of the inactive quadrant. The horizontal wind speed was weak in the eye of the TC, which is an area of calm winds. The maximum horizontal wind speed was at a radius of about 100 km (Figure 8f–j). The maximum wind radius was larger than usual for a TC, maybe due to the coarse resolution of the reanalysis dataset. There was a positive temperature anomaly in the mid- and upper layers (from 500 to 200 hPa), which is characteristic of the warm inner core of a TC. The warm inner core was initially weak and then gradually enhanced (Figure 8k–o). This analysis shows that the fields in the 0–16-day window from the ERA5 dataset better capture the structure and evolution of *Damrey*, but there were also some shortcomings, such as the underestimation of the low-level horizontal wind speed and inaccuracies in describing the radius of maximum horizontal wind speed. However, these shortcomings did not affect our ability to understand the development of the kinetic energy and the contribution of the MG.

3.2.3 | Energetics transfer during intensification of typhoon *Damrey*

What part did the large-scale cyclonic circulation system of the MG play in the development of the TC and how much did it contribute to the kinetic energy of *Damrey*? This was examined to help us to understand the dynamics of the intensification of this TC.

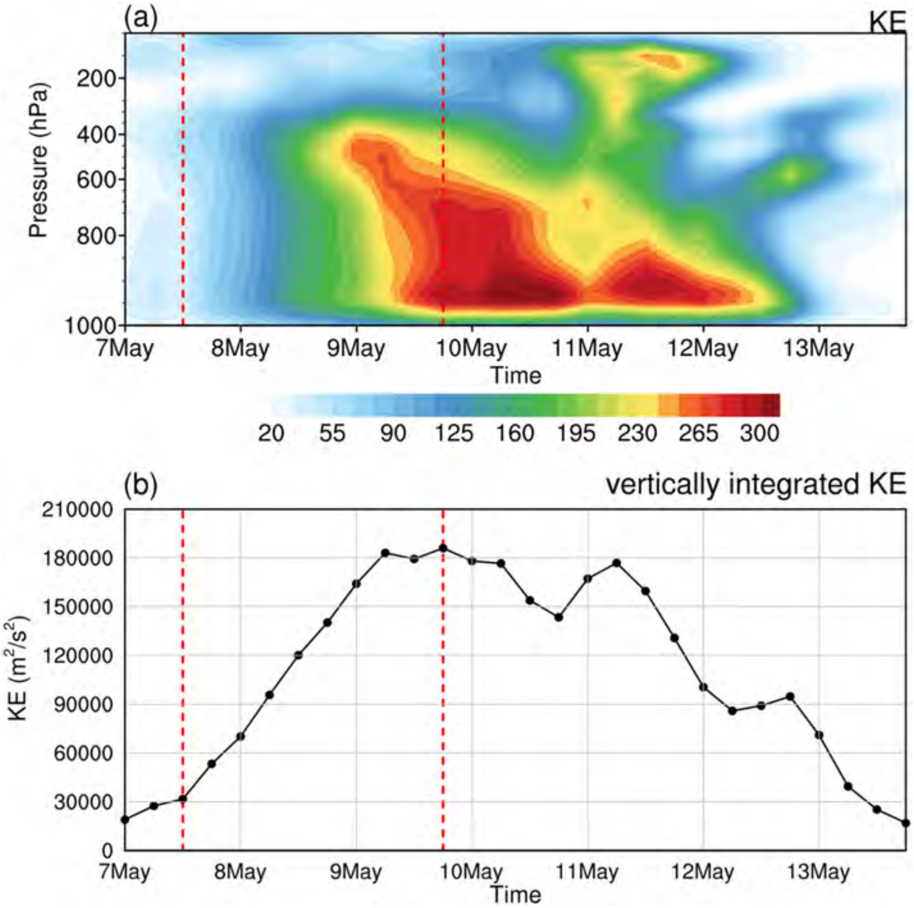

FIGURE 6 (a) Time–pressure cross-section of the kinetic energy (m^2·s^{-2}) on the TC scale averaged over the circle of radius 150 km. (b) Time series (year 2000) of the kinetic energy (m^2·s^{-2}) on the TC scale integrated from 1,000 to 200 hPa for the cylinder of radius 150 km [Colour figure can be viewed at wileyonlinelibrary.com]

Figure 9 shows the profiles of canonical kinetic energy transfer between the three different scale windows from 1800 UTC on 7 May to 1800 UTC on 9 May. Nonlinear interactions between multiscale systems can result in an energy cascade. $\Gamma_n^{0\to 2}$ (Figure 9, TK02) was very small and the large-scale background field did not contribute to the development of the TC during the intensification phase. $\Gamma_n^{0\to 2}$ slightly weakened the kinetic energy in the active quadrant of precipitation and slightly enhanced the kinetic energy in the inactive quadrant of precipitation at 1800 UTC on 9 May, which weakened the asymmetry of the TC and maintained its intensity. $\Gamma_n^{0\oplus 1\to 2}$ (Figure 9, TK012) and $\Gamma_n^{2\to 2}$ (Figure 9, TK22) were both negligible. Meanwhile, the MG contributed a little to the asymmetry of the kinetic energy of the TC. $\Gamma_n^{1\to 2}$ occurred at a height of 850–200 hPa with a centre at 200–400 hPa.

From 0600 UTC on 8 May to 0600 UTC on 9 May, *Damrey* was located in the south of the MG, close to its centre (Figure 3). At 0600 UTC on 9 May, the centre of the TC coincided with the centre of the MG (Figure 3) and $\Gamma_n^{1\to 2} > 0$ in the active quadrant. This means that canonical kinetic energy was transferred from the MG to the TC. By contrast, in the inactive quadrant, $\Gamma_n^{1\to 2} < 0$, which means that kinetic energy was transferred from the TC to the MG, increasing the asymmetry of *Damrey*. In other words, the MG did not favour the intensification of the TC during the intensification phase, consistent with previous statistical results (Liang *et al.*, 2018a; Song *et al.*, 2021). At 1800 UTC on 9 May, *Damrey* was located in the northeast of the MG. $\Gamma_n^{1\to 2} < 0$ in the active quadrant and $\Gamma_n^{1\to 2} > 0$ in the inactive quadrant, which weakened the asymmetry of the TC and maintained its intensity.

Figure 10 shows that the buoyancy conversion ($-b^{\varpi}$; Figure 10, BUOY) was almost symmetrically positive near the eyewall from 400 to 150 hPa in both the active and inactive quadrants – that is, the ascending warmer air parcel near the eyewall caused the TC-scale APE to convert to TC-scale kinetic energy, thus increasing the kinetic energy of the TC. Within the eye of *Darmey*, sinking motion caused the TC-scale kinetic energy to convert to TC-scale APE, thus reducing the kinetic energy of the TC. However, the kinetic energy lost in the eye was much less than the kinetic energy produced in the eyewall by buoyancy conversion.

It is interesting that $-\nabla \cdot Q_P^{\varpi} < 0$ (Figure 10f–j) above 400 hPa near the eyewall, which offset the positive buoyancy conversion (Figure 10k–o), whereas $-\nabla \cdot Q_P^{\varpi} > 0$

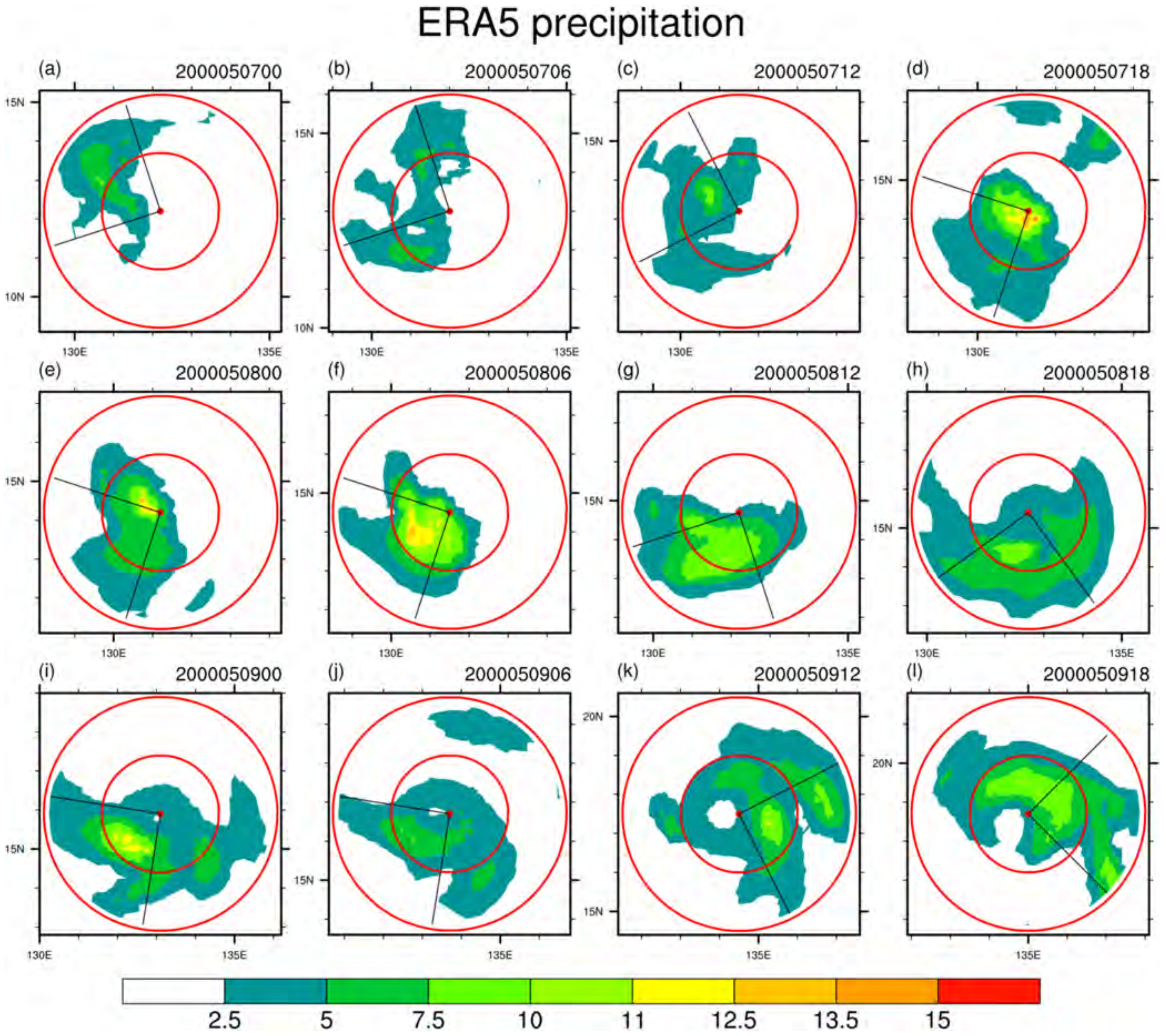

FIGURE 7 Distribution of precipitation (mm·hr^{-1}) during the intensification of *Damrey* from 0000 UTC 7 May to 1800 UTC 9 May. The red dots are the centre of *Damrey* determined in the ERA5 dataset. The red circles have radii of 150 and 300 km, respectively. The 90° sector delineated in black is the precipitation active quadrant [Colour figure can be viewed at wileyonlinelibrary.com]

above 400 hPa inside the eye, which offset the negative buoyancy conversion. In other words, air expanded near the eyewall above 400 hPa and the pressure gradient force carried out negative work (the TC lost kinetic energy), which offset the kinetic energy generated by buoyancy conversion. This means that buoyancy conversion cannot contribute directly to the intensification of the TC.

Below 400 hPa, especially in the lower layer, the air contracted in the active quadrant, related to the inflow, which contributed to intensification of the TC until 0600 UTC on 9 May. By contrast, the air in the inactive quadrant and near the surface within the eye expanded, related to the outflow, which weakened the intensity of the TC until 0600 UTC on 9 May. The positive value was larger than the negative value below 400 hPa, so the air contracting (or inflowing) in the active quadrant was the direct reason for the intensification of *Damrey*. At 1800 UTC on 9 May, the contribution of $-\nabla \cdot Q_P^{\varpi}$ reversed below 400 hPa, apart from on the surface within the eye, and the TC weakened rapidly.

To further understand the mechanisms behind the intensification of *Damrey*, we decomposed the work of the pressure gradient force into the work of the horizontal and vertical directions. In the horizontal direction (Figure 11, third row), the pressure gradient force did positive work in

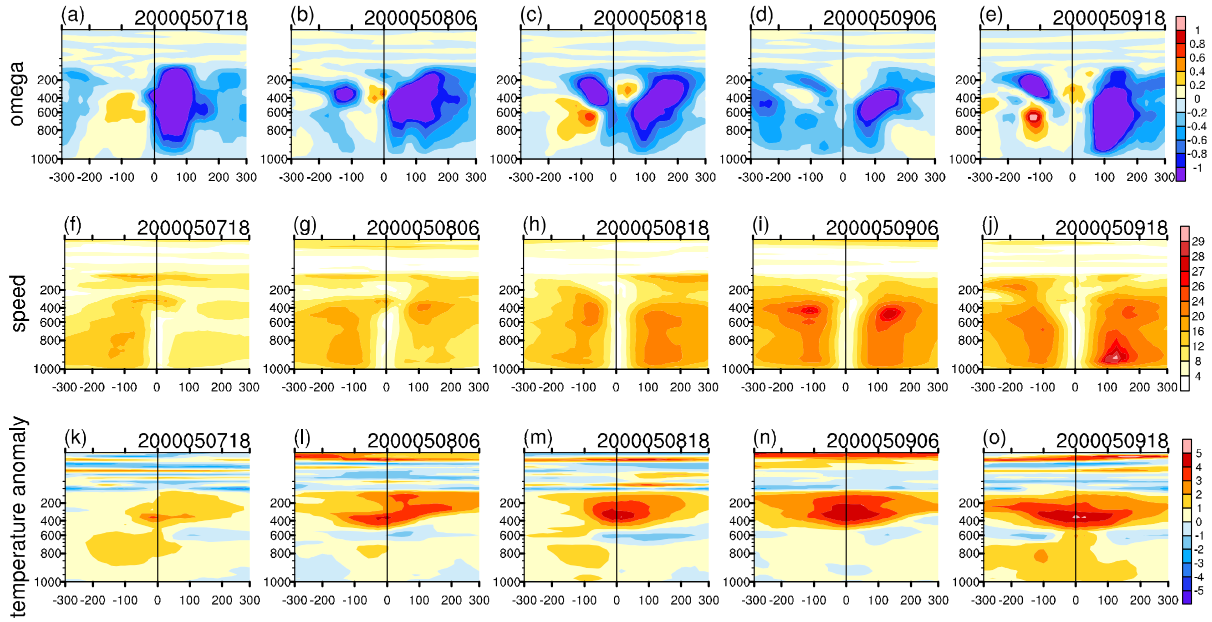

FIGURE 8 Radius–pressure cross-sections of the (a–e) quadrant-mean omega (first row; Pascal·s^{-1}), (f–j) horizontal wind speed (second row; m·s^{-1}) and (k–o) temperature anomaly (third row; K) on the TC scale at 1800 UTC 7 May (first column), 0600 UTC 8 May (second column), 1800 UTC 8 May (third column), 0600 UTC 9 May (fourth column) and 1800 UTC 9 May (fifth column). The positive (negative) *x*-axis is the precipitation active (inactive) quadrant [Colour figure can be viewed at wileyonlinelibrary.com]

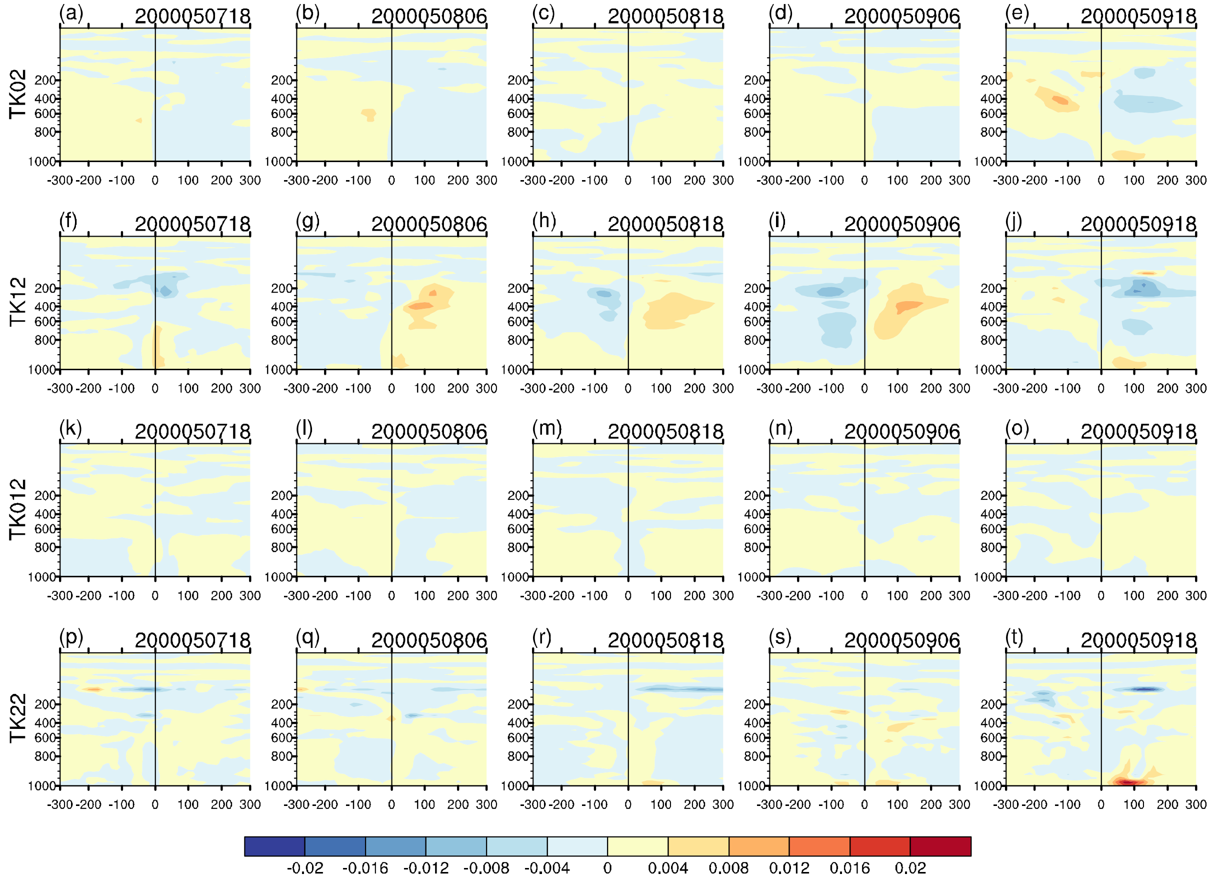

FIGURE 9 Radius–pressure cross-sections of the (a–e) quadrant-mean $\Gamma_n^{0\to2}$ (first row; m^2·s^{-3}), (f–j) $\Gamma_n^{1\to2}$ (second row; m^2·s^{-3}), (k–o) $\Gamma_n^{0\oplus1\to2}$ (third row; m^2·s^{-3}) and (p–t) $\Gamma_n^{2\to2}$ (fourth row; m^2·s^{-3}), on the TC scale at 1800 UTC 7 May (first column), 0600 UTC 8 May (second column), 1800 UTC 8 May (third column), 0600 UTC 9 May (fourth column) and 1800 UTC 9 May (fifth column). The positive (negative) *x*-axis is the precipitation active (inactive) quadrant [Colour figure can be viewed at wileyonlinelibrary.com]

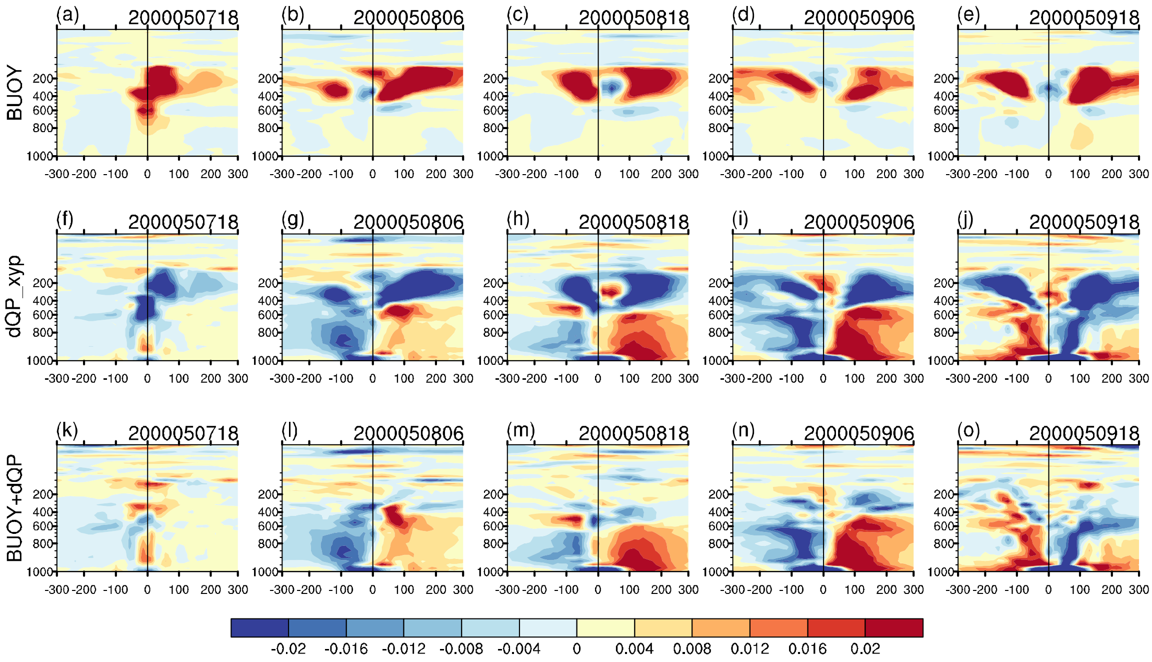

FIGURE 10 Radius–pressure cross-sections of the (a–e) quadrant-mean buoyancy conversion (first row; $m^2 \cdot s^{-3}$), (f–j) pressure-work (second row; $m^2 \cdot s^{-3}$) and (k–o) their sum (third row; $m^2 \cdot s^{-3}$) on the TC scale at 1800 UTC 7 May (first column), 0600 UTC 8 May (second column), 1800 UTC 8 May (third column), 0600 UTC 9 May (fourth column) and 1800 UTC 9 May (fifth column). The positive (negative) *x*-axis is the precipitation active (inactive) quadrant [Colour figure can be viewed at wileyonlinelibrary.com]

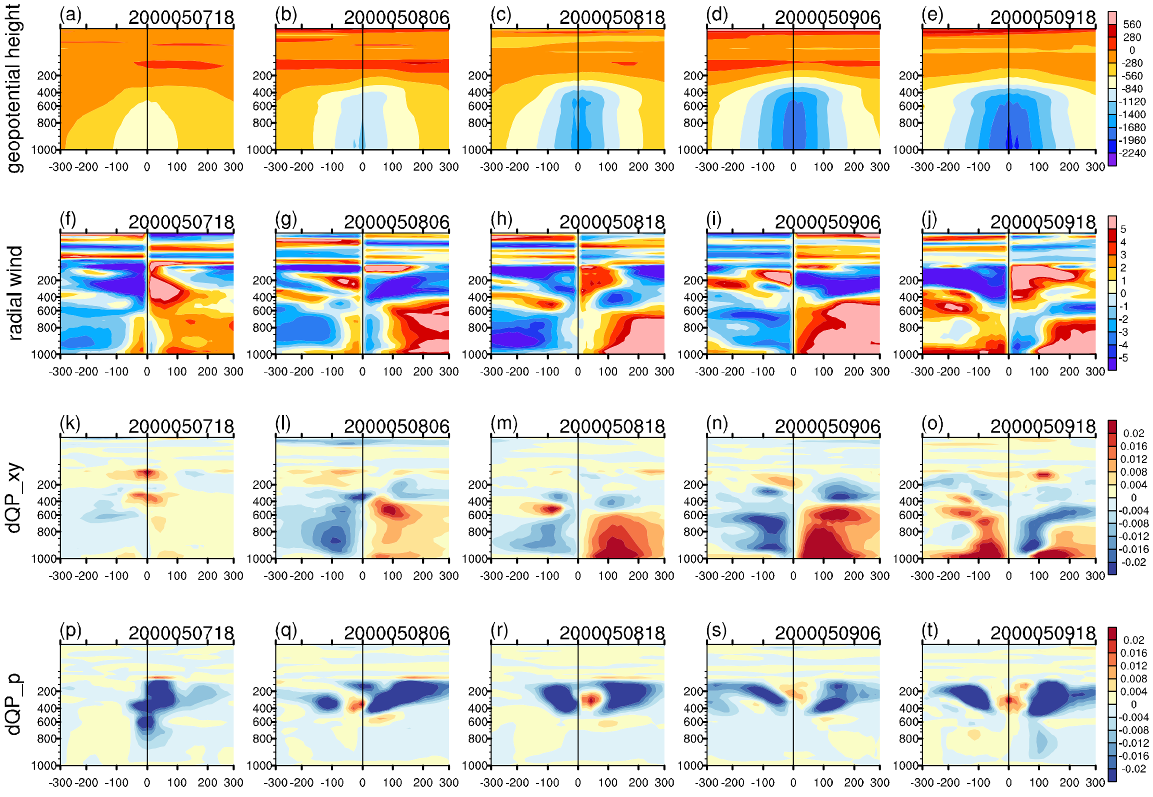

FIGURE 11 Radius–pressure cross-sections of (a–e) the quadrant-mean geopotential height on the TC scale (first row; $m^2 \cdot s^{-2}$), (f–j) the radial wind on the TC scale (second row; $m \cdot s^{-1}$), (k–o) the work done by pressure gradient force in the horizontal direction (third row; $m^2 \cdot s^{-3}$) and (p–t) the work done by pressure gradient force in the vertical direction (fourth row; $m^2 \cdot s^{-3}$), at 1800 UTC 7 May (first column), 0600 UTC 8 May (second column), 1800 UTC 8 May (third column), 0600 UTC 9 May (fourth column) and 1800 UTC 9 May (fifth column). The positive (negative) *x*-axis is the precipitation active (inactive) quadrant [Colour figure can be viewed at wileyonlinelibrary.com]

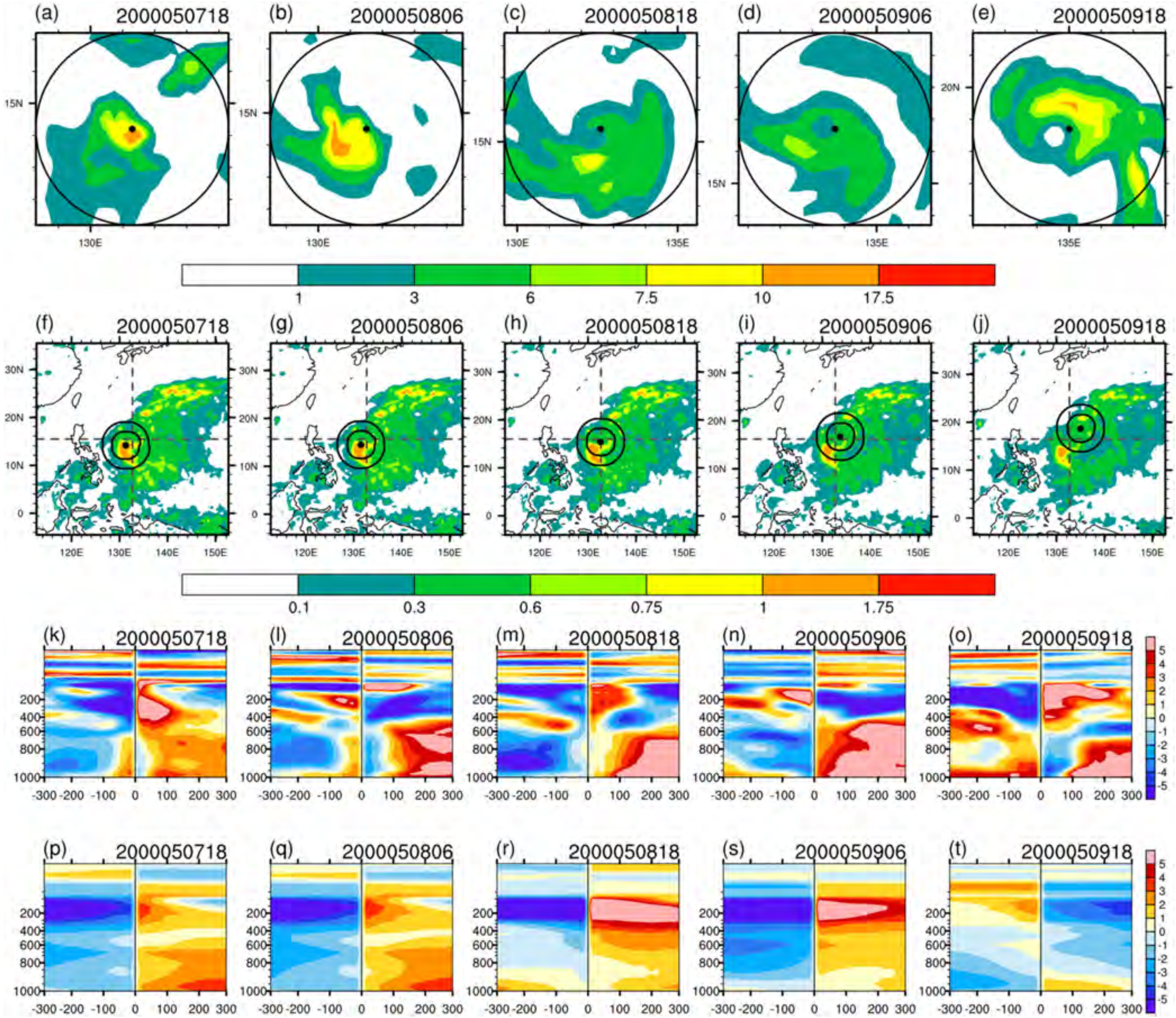

FIGURE 12 Distribution of precipitation on the TC scale (first row; mm·hr^{-1}) and on the MG scale (second row; mm·hr^{-1}). The black circles have radii of 300 km in (a–e), and radii of 300 and 500 km in (f–j). Radius–pressure cross-sections of the quadrant-mean radial wind (k–o) on the TC scale (third row; m·s^{-1}) and (p–t) on the MG scale (fourth row; m·s^{-1}), at 1800 UTC 7 May (first column), 0600 UTC 8 May (second column), 1800 UTC 8 May (third column), 0600 UTC 9 May (fourth column) and 1800 UTC 9 May (fifth column). The positive (negative) *x*-axis is the precipitation active (inactive) quadrant [Colour figure can be viewed at wileyonlinelibrary.com]

the active quadrant with the inflow from the high-pressure area to the centre of *Damrey*, especially during intensification. The horizontal pressure work in the lower layer was much larger than that in the upper layer because the horizontal geopotential gradient in the lower layer was larger than that in the upper layer (Figure 11, first row). The negative work due to the outflow ($u_r < 0$; Figure 11, second row) in the inactive quadrant was much less than the positive work due to the inflow ($u_r > 0$) in the lower troposphere of the active quadrant. In other words, the inflow in the lower layer was the main source of energy for *Damrey*, which is consistent with previous studies (Pendergrass and Willoughby, 2009; Vigh and Schubert, 2009; Montgomery and Smith, 2014). In the vertical direction (Figure 11, fourth row), the pressure gradient force did negative work with the ascending motion from the low-pressure area to the high-pressure area and the vertical pressure work term in the upper layer was much larger than that in the lower layer. This was because the vertical geopotential gradient in the upper layer was larger than that in the lower layer (Figure 11, first row), reiterating the finding that the updraught in the active quadrant offset the kinetic energy produced by buoyancy conversion above 400 hPa.

As previous studies suggested, there are two mechanisms for the radial inflow in the lower troposphere. The inflow outside the eye above the boundary layer is induced by the inner-core convection. The inner-core convection can form a warm core, lower pressure in TC's eye, and force secondary circulation with inflow below the heating maximum and outflow above it (Pendergrass and Willoughby, 2009; Vigh and Schubert, 2009). The inflow can spin up the vortex with the approximate material conservation of absolute angular momentum. On the other hand, Montgomery and Smith (2014) highlighted the role of the inflow within the boundary layer, which is induced by boundary-layer friction and generates maximum super-gradient winds on top of the boundary layer, on the vortex spinning up. Our study verified the local asymmetric inflow in the lower layer contributing to *Damrey*'s intensification.

In order to further investigate the contribution from the MG to *Damrey*'s intensification, the MG-scale radial inflow and precipitation are given in Figure 12, as well as the TC-scale radial inflow and precipitation. It is found that the MG-scale precipitation was much less than the TC-scale precipitation. Its intensity was only about one-tenth of the TC-scale precipitation. At 1800 UTC on 7 May, the MG-scale inflow was obvious in the lower layer of the active quadrant (Figure 12p), but the horizontal pressure gradient was very weak (Figure 11a); the work done by the MG-scale inflow was little. At 0600 UTC on 8 May, the MG-scale inflow was much less than the TC-scale inflow (Figure 12q); the work done by the MG-scale inflow was also much less. From 1800 UTC on 8 May to 0600 UTC on 9 May, the MG-scale inflow was mostly located above 400 hPa, where the horizontal pressure gradient was little (Figure 11c,d), so MG-scale inflow has a negligible contribution to *Damrey*'s intensification.

We conclude from this analysis that the most important source of kinetic energy in the TC was the inflow in the lower troposphere, rather than the buoyancy conversion above 400 hPa, which was offset by the negative work done by the pressure gradient force with the updraught near the eyewall. This conclusion has long been acknowledged, but the concept that the APE generated by buoyancy conversion will convert to kinetic energy and contribute to intensification of the TC is also popular. Here, we confirm that the buoyancy conversion above 400 hPa is not the source of kinetic energy for the TC.

We found that the large-scale background field contributed little to the evolution of the TC, whereas the MG

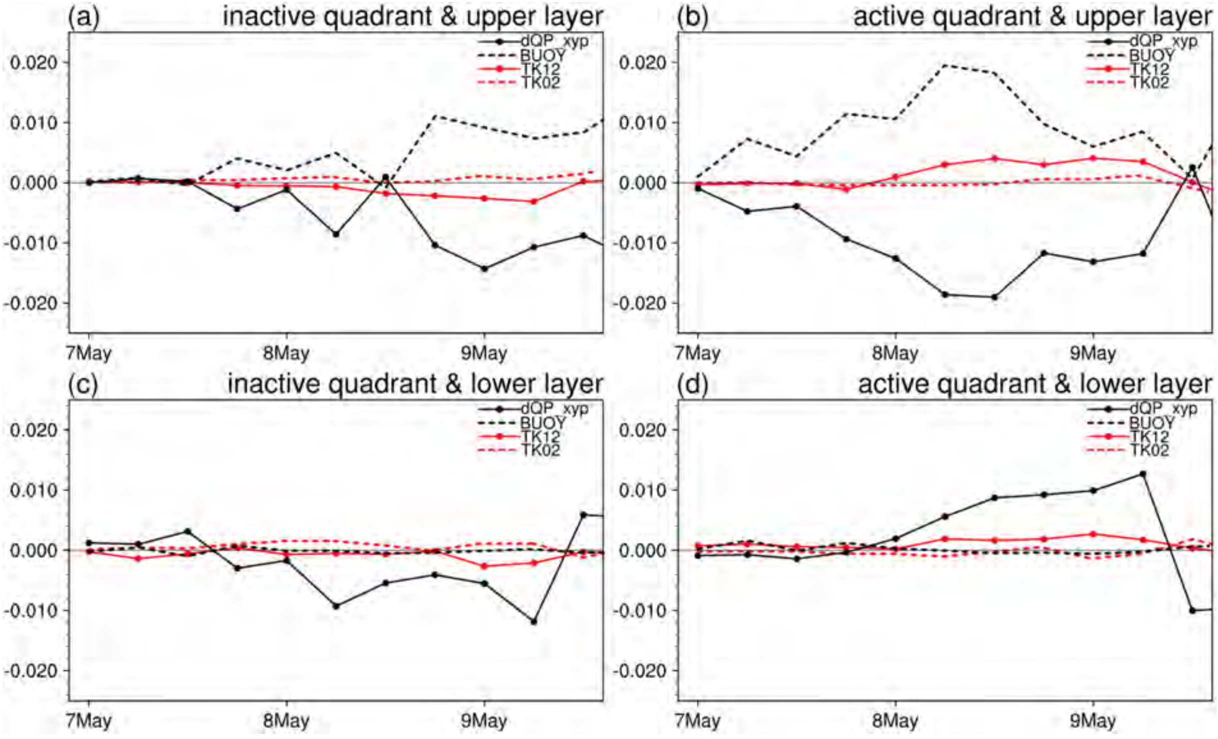

FIGURE 13 Time series of the sector-mean energy budget terms with a radius of 300 km in (a,b) the upper troposphere (vertically averaged from 500 to 200 hPa; first row) and (c,d) the lower troposphere (vertically averaged from 1,000 to 500 hPa; second row) for the precipitation inactive quadrant (a,c) and the precipitation active quadrant (b,d). Black solid line is $-\nabla \cdot Q_P^{\varpi}$ (denoted by dQP_xyp; $m^2 \cdot s^{-3}$), black dashed line is $-b^{\varpi}$(denoted by BUOY; $m^2 \cdot s^{-3}$), red solid line is $\Gamma_n^{1\to 2}$ (denoted by TK12; $m^2 \cdot s^{-3}$) and red dashed line is $\Gamma_n^{0\to 2}$(denoted by TK02; $m^2 \cdot s^{-3}$) [Colour figure can be viewed at wileyonlinelibrary.com]

contributed to the asymmetry. In the next subsection, it will be further shown that the canonical transfer (that is, barotropic conversion) term was not the main source of energy for the rapid intensification of the TC, whereas the inflow at the lower level had an important role in the development of the TC.

3.2.4 | Contribution of each term

The characteristics of the energetics are different in the upper and lower troposphere and in the active and inactive quadrants. We therefore divided the TC into four regions with 500 hPa as the interface: an upper inactive quadrant; a lower inactive quadrant; an upper active quadrant; and a lower active quadrant. We then integrated and averaged the energy contribution in these different quadrants (Figure 13).

It is clear that the $-b^{\varpi}$ and $-\nabla \cdot Q_P^{\varpi}$ terms almost offset each other in the upper troposphere (Figure 13). By contrast, in the lower troposphere, $-\nabla \cdot Q_P^{\varpi}$ made the dominant contribution as a result of inflow or outflow. $-\nabla \cdot Q_P^{\varpi}$ contributed positively in the active quadrant from 0000 UTC on 8 May to 0600 UTC on 9 May, then its contribution decreased rapidly to negative. $-\nabla \cdot Q_P^{\varpi}$ contributed negatively in the inactive quadrant at low levels from 1800 UTC on 7 May to 0600 UTC on 9 May.

As a result of the offset of $-\nabla \cdot Q_P^{\varpi}$ and $-b^{\varpi}$ in the upper troposphere, we combined them (Figure 14, BUOY+dQP) for comparison with the other terms. The term $-\nabla \cdot Q_P^{\varpi} - b^{\varpi}$ was negative in the upper troposphere from 0000 UTC on 8 May to 0600 UTC on 9 May

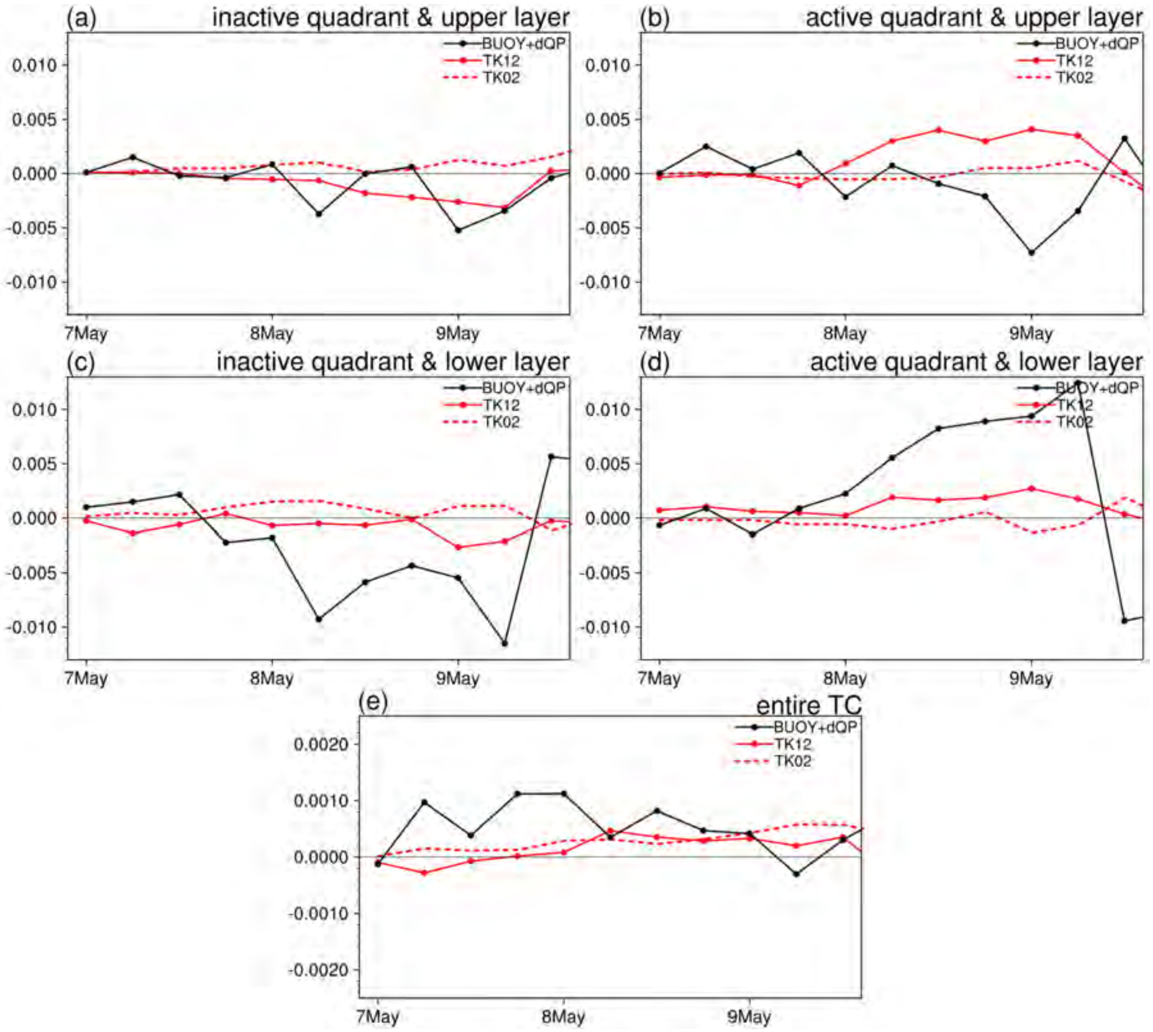

FIGURE 14 Time series of the sector-mean energy budget terms with a radius 300 km in (a,b) the upper troposphere (vertically averaged from 500 to 200 hPa; first row) and (c,d) the lower troposphere (vertically averaged from 1,000 to 500 hPa; second row) for the precipitation inactive quadrant (a,c) and the precipitation active quadrant (b,d). (e) Time series of the azimuthal-mean energy budget terms of the average over the cylinder of radius 300 km. Black line is the sum of $-b^{\varpi}$ and $-\nabla \cdot Q_P^{\varpi}$ ($\mathrm{m^2{\cdot}s^{-3}}$), red solid line is $\Gamma_n^{1\to2}$ ($\mathrm{m^2{\cdot}s^{-3}}$) and red dashed line is $\Gamma_n^{0\to2}$ ($\mathrm{m^2{\cdot}s^{-3}}$) [Colour figure can be viewed at wileyonlinelibrary.com]

due to the updraught. $-b^{\varpi}$ was negligible in the lower troposphere (Figure 13c,d) and the value of $-\nabla \cdot Q_P^{\varpi} - b^{\varpi}$ was determined by $-\nabla \cdot Q_P^{\varpi}$, which made a positive contribution due to inflow in the active quadrant and a negative contribution due to outflow in the inactive quadrant. For the canonical transfer terms, $\Gamma_n^{1\to2}$ contributed positively to the kinetic energy of *Damrey* in the active quadrants from 0000 UTC on 8 May to 1200 UTC on 9 May (Figure 14b,d). By contrast, in the inactive quadrant, $\Gamma_n^{1\to2}$ contributed negatively to the kinetic energy (Figure 14a,c), whereas $\Gamma_n^{0\to2}$ was negligible. The results were consistent if the 180° azimuthal average was used to define the active and inactive quadrants (Figure S4).

If we consider the kinetic energy of the whole typhoon – that is, without quadrant division – then $\Gamma_n^{1\to2}$ had a minor role in contributing to the development of the whole TC, slightly reducing the kinetic energy on 7 May and increasing it on 8 May, whereas the term $-\nabla \cdot Q_P^{\varpi} - b^{\varpi}$ made a significant positive contribution to the intensification of *Damrey* (Figure 14e).

4 | CONCLUSIONS

Based on the MWT developed by Liang and Anderson (2007), we examined the multiscale dynamical processes and energy sources of typhoon *Damrey*. This was the first named TC of 2000 and was embedded in an MG during its period of rapid intensification from 0600 UTC on 8 May to 0600 UTC on 9 May. *Damrey* was located in the periphery of the subtropical high and moved into the westerly jet at mid- and high levels after 10 May.

We decomposed and reconstructed the reanalysis fields from the ERA5 dataset into three temporal scales: a background window (>64 days); an MG-scale window (16–64 days); and a TC-scale window (<16 days). We then applied the MWT-based localized and instantaneous multiscale energetics analysis developed by Liang and Robinson (2005) and Liang (2016). We found that the buoyancy conversion term did positive work in the upper troposphere – that is, the APE was converted to the kinetic energy of the TC. However, the negative work done by the vertical pressure gradient force with the updraught near the eyewall in the upper troposphere offset the positive work of buoyancy conversion. The important source of production of kinetic energy in *Damrey* was therefore the positive work done by the horizontal pressure gradient force due to inflow in the lower troposphere.

We found that the large-scale background field contributed little to the evolution of the TC, whereas the MG contributed to its asymmetry. The MG increased the kinetic energy in the precipitation active quadrant and weakened the kinetic energy in the precipitation inactive quadrant. Canonical transfer – that is, the barotropic conversion term – was therefore not the main energy source in the rapid intensification of the TC. By contrast, the inflow in the lower troposphere had played an important role in the intensification of the TC, consistent with the WISHE mechanism.

Although the (0.25° × 0.25°) resolution of the reanalysis dataset is fairly coarse, these findings will help us to understand the impact of MGs on the intensification of TCs and their underlying mechanisms of evolution.

AUTHOR CONTRIBUTIONS

Kexin Song: Data curation; formal analysis; methodology; visualization; writing – original draft. **Li Tao:** Conceptualization; methodology; supervision; writing – review and editing. **Yang Yang:** Methodology; writing – review and editing.

ACKNOWLEDGEMENTS

This work was funded by the Key Program of National Natural Science Foundation of China under grant 42230105. the Open Grants of the State Key Laboratory of Severe Weather under grant 2022LASW-B07 and the National Science Foundation of China under grant 42276017 and 41975064.

ORCID

Kexin Song https://orcid.org/0000-0003-4536-0512
Li Tao https://orcid.org/0000-0002-2644-983X

REFERENCES

Bui, H.H., Smith, R.K., Montgomery, M.T. and Peng, J. (2009) Balanced and unbalanced aspects of tropical cyclone intensification. *Quarterly Journal of the Royal Meteorological Society*, 135, 1715–1731.

Carr, L.E. and Elsberry, R.L. (1995) Monsoonal interactions leading to sudden tropical cyclone track changes. *Monthly Weather Review*, 123, 265–290.

Charney, J.G. and Eliassen, A. (1964) On the growth of the hurricane depression. *Journal of Atmospheric Sciences*, 21, 68–75.

Chen, X., Wang, Y. and Zhao, K. (2015) Synoptic flow patterns and large-scale characteristics associated with rapidly intensifying tropical cyclones in the South China Sea. *Monthly Weather Review*, 143, 64–87.

Craig, G.C. and Gray, S.L. (1996) CISK or WISHE as the mechanism for tropical cyclone intensification. *Journal of Atmospheric Sciences*, 53(23), 3528–3540.

Emanuel, K.A. (1986) An air-sea interaction theory for tropical cyclones. Part I: steady-state maintenance. *Journal of the Atmospheric Sciences*, 43, 585–605.

Emanuel, K.A. (1989) The finite-amplitude nature of tropical cyclogenesis. *Journal of the Atmospheric Sciences*, 46, 3431–3456.

Emanuel, K.A. (1997) Some aspects of hurricane inner-core dynamics and energetics. *Journal of the Atmospheric Sciences*, 54, 1014–1026.

Fowler, J.P. and Galarneau, T.J. (2017) Influence of storm–storm and storm–environment interactions on tropical cyclone formation and evolution. *Monthly Weather Review*, 145, 4855–4875.

Frank, W.M. and Ritchie, E.A. (2001) Effects of vertical wind shear on the intensity and structure of numerically simulated hurricanes. *Monthly Weather Review*, 129, 2249–2269.

Fujiwhara, S. (1921) The natural tendency towards symmetry of motion and its application as a principle in meteorology. *Quarterly Journal of the Royal Meteorological Society*, 47, 287–292.

Fujiwhara, S. (1923) On the growth and decay of vortical systems. *Quarterly Journal of the Royal Meteorological Society*, 49, 75–104.

Ge, X., Yan, Z., Peng, M., Bi, M. and Li, T. (2018) Sensitivity of tropical cyclone track to the vertical structure of a nearby monsoon gyre. *Journal of the Atmospheric Sciences*, 75, 2017–2028.

Hanley, D., Molinari, J. and Keyser, D. (2001) A composite study of the interactions between tropical cyclones and upper-tropospheric troughs. *Monthly Weather Review*, 129, 2570–2584.

Harr, P.A., Elsberry, R.L. and Chan, J.C.L. (1996) Transformation of a large monsoon depression to a tropical storm during TCM-93. *Monthly Weather Review*, 124, 2625–2643.

Hartmann, D.L. and Maloney, E.D. (2001) The Madden–Julian oscillation, barotropic dynamics, and North Pacific tropical cyclone formation. Part II: stochastic barotropic modeling. *Journal of the Atmospheric Sciences*, 58, 2559–2570.

Hendricks, E.A., Montgomery, M.T. and Davis, C.A. (2004) The role of "vortical" hot towers in the formation of tropical cyclone Diana (1984). *Journal of the Atmospheric Sciences*, 61, 1209–1232.

Heng, J., Wang, Y. and Zhou, W. (2017) Revisiting the balanced and unbalanced aspects of tropical cyclone intensification. *Journal of the Atmospheric Sciences*, 74(8), 2575–2591.

Hersbach, H., Bell, B., Berrisford, P., Hirahara, S., et al. (2020) The ERA5 global reanalysis. *Quarterly Journal of the Royal Meteorological Society*, 146, 1999–2049.

Houze, R.A., Jr., Chen, S.S., Smull, B.F., Lee, W.C. and Bell, M.M. (2007) Hurricane intensity and eyewall replacement. *Science*, 315, 1235–1239.

Kaplan, J. and DeMaria, M. (2003) Large-scale characteristics of rapidly intensifying tropical cyclones in the North Atlantic basin. *Weather and Forecasting*, 18, 1093–1108.

Kaplan, J., DeMaria, M. and Knaff, J.A. (2010) A revised tropical cyclone rapid intensification index for the Atlantic and eastern North Pacific basins. *Weather and Forecasting*, 25, 220–241.

Lander, M.A. (1994) Description of a monsoon gyre and its effects on the tropical cyclones in the western North Pacific during August 1991. *Weather and Forecasting*, 9, 640–654.

Lander, M.A. (1996) Specific tropical cyclone track types and unusual tropical cyclone motions associated with a reverse-oriented monsoon trough in the western North Pacific. *Weather and Forecasting*, 11, 170–186.

Leroux, M.-D., Plu, M., Barbary, D., Roux, F. and Arbogast, P. (2013) Dynamical and physical processes leading to tropical cyclone intensification under upper-level trough forcing. *Journal of the Atmospheric Sciences*, 70, 2547–2565.

Liang, J. and Wu, L. (2015) Sudden track changes of tropical cyclones in monsoon gyres: full-physics, idealized numerical experiments. *Journal of the Atmospheric Sciences*, 72, 1307–1322.

Liang, J., Wu, L. and Gu, G. (2018a) Rapid weakening of tropical cyclones in monsoon gyres over the tropical western North Pacific. *Journal of Climate*, 31, 1015–1028.

Liang, J., Wu, L. and Gu, G. (2018b) Numerical study of the influences of a monsoon gyre on intensity changes of typhoon Chan-Hom (2015). *Advances in Atmospheric Sciences*, 35, 567–579.

Liang, J., Wu, L., Gu, G. and Liu, Q. (2016) Rapid weakening of Typhoon Chan-Hom (2015) in a monsoon gyre. *Journal of Geophysical Research: Atmospheres*, 121, 9508–9520.

Liang, X.S. (2002) *Wavelet-Based Multiscale Window Transform and Energy and Vorticity Analysis*. Cambridge, MA: Harvard Reports in Physical/Interdisciplinary Ocean Science, Rep. No. 66, Harvard University, p. 411.

Liang, X.S. (2016) Canonical transfer and multiscale energetics for primitive and quasigeostrophic atmospheres. *Journal of the Atmospheric Sciences*, 73, 4439–4468.

Liang, X.S. and Anderson, D.G.M. (2007) Multiscale window transform. *Multiscale Modeling & Simulation*, 6, 437–467.

Liang, X.S. and Robinson, A.R. (2005) Localized multiscale energy and vorticity analysis: I. Fundamentals. *Dynamics of Atmospheres and Oceans*, 38, 195–230.

Liang, X.S. and Robinson, A.R. (2007) Localized multi-scale energy and vorticity analysis. II. Finite-amplitude instability theory and validation. *Dynamics of Atmospheres and Oceans*, 44, 51–76.

Liang, X.S. and Robinson, A.R. (2009) Multiscale processes and nonlinear dynamics of the circulation and upwelling events off Monterey Bay. *Journal of Physical Oceanography*, 39, 290–313.

Ma, J. and Liang, X.S. (2017) Multiscale dynamical processes underlying the wintertime Atlantic blockings. *Journal of the Atmospheric Sciences*, 74, 3815–3831.

Ma, Z., Fei, J. and Huang, X. (2019) A definition of rapid weakening for tropical cyclones over the western North Pacific. *Geophysical Research Letters*, 46, 11471–11478.

Maloney, E.D. and Hartmann, D.L. (2001) The Madden–Julian oscillation, barotropic dynamics, and North Pacific tropical cyclone formation. Part I: observations. *Journal of the Atmospheric Sciences*, 58, 2545–2558.

Molinari, J., Vollaro, D., Skubis, S. and Dickinson, M. (2000) Origins and mechanisms of eastern Pacific tropical cyclogenesis: a case study. *Monthly Weather Review*, 128, 125–139.

Montgomery, M.T., Bell, M.M., Aberson, S.D. and Black, M.L. (2006) Hurricane Isabel (2003): new insights into the physics of intense storms. Part I: mean vortex structure and maximum intensity estimates. *Bulletin of the American Meteorological Society*, 87, 1335–1348.

Montgomery, M.T., Sang, N.V., Smith, R.K. and Persing, J. (2009) Do tropical cyclones intensify by WISHE? *Quarterly Journal of the Royal Meteorological Society*, 135, 1697–1714.

Montgomery, M.T. and Smith, R.K. (2014) Paradigms for tropical cyclone intensification. *Australian Meteorological and Oceanographic Journal*, 64, 37–66.

Ooyama, K. (1969) Numerical simulation of the life cycle of tropical cyclones. *Journal of Atmospheric Sciences*, 26, 3–40.

Ooyama, K.V. (1982) Conceptual evolution of the theory and modeling of the tropical cyclone. *Journal of the Meteorological Society of Japan. Ser. II*, 60, 369–379.

Pendergrass, A.G. and Willoughby, H.E. (2009) Diabatically induced secondary flows in tropical cyclones. Part I: quasi-steady forcing. *Monthly Weather Review*, 137, 805–821.

Riemer, M., Montgomery, M.T. and Nicholls, M.E. (2010) A new paradigm for intensity modification of tropical cyclones: thermodynamic impact of vertical wind shear on the inflow layer. *Atmospheric Chemistry and Physics*, 10, 3163–3188.

Schubert, W.H. and Hack, J.J. (1982) Inertial stability and tropical cyclone development. *Journal of the Atmospheric Sciences*, 39, 1687–1697.

Shapiro, L.J. and Willoughby, H.E. (1982) The response of balanced hurricanes to local sources of heat and momentum. *Journal of the Atmospheric Sciences*, 39, 378–394.

Song, K., Tao, L. and Gao, J. (2021) Rapid weakening of tropical cyclones in monsoon gyres over the western North Pacific: a revisit. *Frontiers in Earth Science*, 9, 688613.

Tang, B. and Emanuel, K. (2010) Midlevel ventilation's constraint on tropical cyclone intensity. *Journal of the Atmospheric Sciences*, 67, 1817–1830.

Vigh, J.L. and Schubert, W.H. (2009) Rapid development of the tropical cyclone warm core. *Journal of the Atmospheric Sciences*, 66, 3335–3350.

Wang, B., Xiang, B. and Lee, J.Y. (2013) Subtropical high predictability establishes a promising way for monsoon and tropical storm predictions. *Proceedings of the National Academy of Sciences*, 110, 2718–2722.

Wang, L. and Liang, X.S. (2017) A diagnosis of some dynamical processes underlying a higher-latitude typhoon using the multiscale window transform. *Atmosphere*, 8, 118.

Wang, Y. (2002) Vortex Rossby waves in a numerically simulated tropical cyclone. Part II: the role in tropical cyclone structure and intensity changes. *Journal of Atmospheric Sciences*, 59, 1239–1262.

Wang, Y. (2009) How do outer spiral rainbands affect tropical cyclone structure and intensity? *Journal of Atmospheric Sciences*, 66, 1250–1273.

Willoughby, H.E., Clos, J.A. and Shoreibah, M.G. (1982) Concentric eye walls, secondary wind maxima, and the evolution of the hurricane vortex. *Journal of the Atmospheric Sciences*, 39, 395–411.

Wood, K.M. and Ritchie, E.A. (2015) A definition for rapid weakening of North Atlantic and eastern North Pacific tropical cyclones. *Geophysical Research Letters*, 42, 10091–10097.

Wu, L. and Duan, J. (2015) Extended simulation of tropical cyclone formation in the western North Pacific monsoon trough. *Journal of Atmospheric Sciences*, 72, 4469–4485.

Wu, L., Zong, H. and Liang, J. (2013) Observational analysis of tropical cyclone formation associated with monsoon gyres. *Journal of the Atmospheric Sciences*, 70, 1023–1034.

Wu, Q., Wang, X. and Tao, L. (2020) Interannual and interdecadal impact of western North Pacific subtropical high on tropical cyclone activity. *Climate Dynamics*, 54, 2237–2248.

Xu, F. and Liang, X.S. (2017) On the generation and maintenance of the 2012/13 sudden stratospheric warming. *Journal of Atmospheric Sciences*, 74, 3209–3228.

Xu, F. and Liang, X.S. (2020) The synchronization between the zonal jet stream and temperature anomalies leads to an extremely freezing North America in January 2019. *Geophysical Research Letters*, 47, e2020GL089689.

Xu, F. and Liang, X.S. (2022) Drastic change in dynamics as Typhoon Lekima experiences an eyewall replacement cycle. *Frontiers of Earth Science*, 16(1), 121–131.

Yan, Z., Ge, X., Peng, M. and Li, T. (2019) Does monsoon gyre always favour tropical cyclone rapid intensification? *Quarterly Journal of the Royal Meteorological Society*, 145, 2685–2697.

Yan, Z., Ge, X., Wang, Z., Wu, C.C. and Peng, M. (2021) Understanding the impacts of upper-tropospheric cold low on typhoon Jongdari (2018) using piecewise potential vorticity inversion. *Monthly Weather Review*, 149, 1499–1515.

Yang, Y. and Liang, X.S. (2016) The instabilities and multiscale energetics underlying the mean–interannual–eddy interactions in the Kuroshio extension region. *Journal of Physical Oceanography*, 46, 1477–1494.

Zong, H. and Wu, L. (2015) Re-examination of tropical cyclone formation in monsoon troughs over the western North Pacific. *Advances in Atmospheric Sciences*, 32, 924–934.

SUPPORTING INFORMATION

Additional supporting information can be found online in the Supporting Information section at the end of this article.

How to cite this article: Song, K., Tao, L. & Yang, Y. (2023) On the intensification of typhoon *Damrey* with the monsoon gyre. *Quarterly Journal of the Royal Meteorological Society*, 149(751), 588–607. Available from: https://doi.org/10.1002/qj.4425